







# A joint 2- and 3-point clustering analysis of the VIPERS PDR2 catalogue at $z \sim 1$ : breaking the degeneracy of cosmological parameters

Alfonso Veropalumbo <sup>1,2★</sup>, Iñigo Sáez Casares,<sup>3</sup> Enzo Branchini <sup>1,2,4</sup>, Benjamin R. Granett <sup>5,6,7</sup>,  
Luigi Guzzo,<sup>5,6,7</sup> Federico Marulli <sup>8,9,10</sup>, Michele Moresco <sup>8,9</sup>, Lauro Moscardini <sup>8,9,10</sup>,  
Andrea Pezzotta<sup>11,12,13</sup> and Sylvain de la Torre<sup>14</sup>

<sup>1</sup>Dipartimento di Matematica e Fisica, Università degli studi Roma Tre, via della Vasca Navale 84, I-00146 Roma, Italy

<sup>2</sup>INFN – Sezione di Roma Tre, via della Vasca Navale 84, I-00146 Roma, Italy

<sup>3</sup>École Normale Supérieure Paris-Saclay, 4 avenue des Sciences, F-91190 Gif-sur-Yvette, France

<sup>4</sup>INAF – Osservatorio Astronomico di Roma, via Frascati 33, I-00040 Monte Porzio Catone (RM), Italy

<sup>5</sup>INAF – Osservatorio Astronomico di Brera, via Brera 28, I-20122 Milano, Italy

<sup>6</sup>INAF – Osservatorio Astronomico di Brera, via E. Bianchi 46, I-23807 Merate, Italy

<sup>7</sup>Università degli Studi di Milano, via G. Celoria 16, I-20133 Milano, Italy

<sup>8</sup>Dipartimento di Fisica e Astronomia “Augusto Righi” – Alma Mater Studiorum Università di Bologna, via Piero Gobetti 93/2, I-40129 Bologna, Italy

<sup>9</sup>INAF – Osservatorio di Astrofisica e Scienza dello Spazio di Bologna, via Piero Gobetti 93/3, I-40129 Bologna, Italy

<sup>10</sup>INFN – Sezione di Bologna, viale Berti Pichat 6/2, I-40127 Bologna, Italy

<sup>11</sup>Max-Planck-Institut für extraterrestrische Physik, Postfach 1312, Giessenbachstr, D-85741 Garching, Germany

<sup>12</sup>Institute of Space Sciences (ICE CSIC), Campus UAB, Carrer de Can Magrans s/n, E-08193 Barcelona, Spain

<sup>13</sup>Institut d’Estudis Espacials de Catalunya (IEEC), E-08034 Barcelona, Spain

<sup>14</sup>Aix Marseille Univ, CNRS, CNES, LAM, F-13388 Marseille, France

Accepted 2021 July 28. Received 2021 July 28; in original form 2021 June 22

## ABSTRACT

We measure the galaxy two- and three-point correlation functions at  $z = [0.5, 0.7]$  and  $z = [0.7, 0.9]$ , from the Public Data Release 2 (PDR2) of the VIMOS Public Extragalactic Redshift Survey (VIPERS). We model the two statistics including a non-linear one-loop model for the two-point function and a tree-level model for the three-point function, and perform a joint likelihood analysis. The entire process and non-linear corrections are tested and validated through the use of the 153 highly realistic VIPERS mock catalogues, showing that they are robust down to scales as small as  $10 h^{-1}$  Mpc. The mocks are also adopted to compute the covariance matrix that we use for the joint two- and three-point analysis. Despite the limited statistics of the two (volume-limited) subsamples analysed, we demonstrate that such a combination successfully breaks the degeneracy existing at two-point level between clustering amplitude  $\sigma_8$ , linear bias  $b_1$ , and the linear growth rate of fluctuations  $f$ . For the latter, in particular, we measure  $f(z = 0.61) = 0.64^{+0.55}_{-0.37}$  and  $f(z = 0.8) = 1.0 \pm 1.0$ , while the amplitude of clustering is found to be  $\sigma_8(z = 0.61) = 0.50 \pm 0.12$  and  $\sigma_8(z = 0.8) = 0.39^{+0.11}_{-0.13}$ . These values are in excellent agreement with the extrapolation of a *Planck* cosmology.

**Key words:** galaxies: statistics – large-scale structure of Universe – cosmology: observations.

## 1 INTRODUCTION

Galaxy clustering has emerged over the past three decades as one main observational pillar supporting the current standard model of cosmology. Cosmological constraints were so far derived mostly from two-point statistics of the galaxy distribution, either in configuration or in Fourier space (see e.g. Alam et al. 2021, for a comprehensive recent review). Two-point statistics will remain a central probe also for the next generation of redshift surveys, which have just started or are about to start. This includes in particular the measurement of specific features, as baryonic acoustic oscillations (BAO; e.g. Cole et al. 2005; Eisenstein et al. 2005) and redshift-space distortions (RSDs; e.g. Peacock et al. 2001; Guzzo et al. 2008),

which are part of the standard ‘dark energy’ probes in projects like Dark Energy Spectroscopic Instrument (DESI; DESI Collaboration 2016a,b), the *Euclid* (Laureijs et al. 2011), and *Roman* (Akeson et al. 2019) space telescopes or, in the radio, the Square Kilometre Array (SKA; Maartens et al. 2015).

For a Gaussian random field, this would be enough to fully characterize the field statistically. However, significant information exists in the galaxy distribution, beyond the two-point correlation function (2PCF) or the power spectrum. This is locked in the  $n$ -point correlation functions, or higher moments, of the field. The simplest of these, the three-point correlation function (3PCF), is sensitive to non-Gaussian features in the primordial density perturbations, non-linear effects in their evolution, and galaxy biasing, i.e. the relationship between galaxy tracers and the underlying distribution of matter. Since these effects are characterized by a different higher order signal (see e.g. Fry 1994; Matarrese, Verde & Heavens 1997),

\* E-mail: [alfonso.veropalumbo@uniroma3.it](mailto:alfonso.veropalumbo@uniroma3.it)

the measurements of the 3PCF (or equivalently in Fourier space, the bispectrum) have the potential to separate them and constrain their relative strength and evolution. In addition, BAO and RSD also leave an imprint on higher order statistics that can be exploited to remove parameter degeneracy and improve cosmological constraints.

The advantage of combining two- and three-point statistics to improve cosmological constraints has been realized in recent years (Sefusatti et al. 2006; Yankelevich & Porciani 2019). These works showed that the combination of the 3D power spectrum and bispectrum can significantly reduce statistical errors in the determination of cosmological parameters, while breaking degeneracies among these. The benefit is remarkable when using clustering data alone. These considerations have inspired the recent combined two- and three-point analyses on Sloan Digital Sky Survey (SDSS) data carried out by Gil-Marín et al. (2015, 2017).

In configuration space, the measurement of the 3PCF is computationally more demanding. Examples in the literature include estimates from the 2dF Galaxy Redshift Survey (2dFGRS; Jing & Börner 2004), various releases of the SDSS main sample (Kayo et al. 2004; Nichol et al. 2006; Kulkarni et al. 2007; McBride et al. 2011a,b; Marín 2011; Guo et al. 2014), the Baryon Oscillation Spectroscopic Survey (BOSS) CMASS (Guo et al. 2015), and the Public Data Release 1 (PDR1) of the VIMOS Public Extragalactic Redshift Survey (VIPERS; Moresco et al. 2017). Only recently, however, thanks to a breakthrough in the efficiency of available estimators, it has become possible to push measurements of the 3PCF to scales comparable to those of the BAO peak (Slepian & Eisenstein 2015; Slepian et al. 2017a,b), also using galaxy clusters as tracers (Moresco et al. 2020). Finally, combined 2PCF and 3PCF analyses in configuration space were performed by Marín et al. (2013) using the WiggleZ spectroscopic galaxy survey.

In this paper, we perform for the first time a joint two- and three-point correlation analysis of the Public Data Release 2 (PDR2) catalogue of the VIPERS (Garilli et al. 2014; Guzzo et al. 2014; Scodreggio et al. 2018), applying the most advanced estimators and extracting joint cosmological constraints out to  $z = 0.9$ . One main goal of VIPERS was to constrain the growth rate of structure  $f$  out to  $z \sim 1$ , a result that was successfully achieved through a series of complementary estimates (de la Torre et al. 2013, 2017; Pezzotta et al. 2017; Mohammad et al. 2018). All these analyses were developed in configuration space, for which the survey geometry and footprint can be more easily handled, if compared to the complex window function convolution one has to deal with in Fourier space (Rota et al. 2017). The main drawback when working in configuration space is the large covariance of 2PCF and 3PCF data and their errors. However, thanks to the availability of efficient clustering estimators and of the large ensemble of realistic mock catalogues made available by the VIPERS Collaboration (de la Torre et al. 2017), we can solve the problem by numerically estimating the covariance matrix of the data.

We thus build upon previous VIPERS analyses to perform a joint 2PCF and 3PCF measurement, which allows us to break the degeneracy that affects some key cosmological parameters when these are estimated from the 2PCF alone. Specifically, we obtain separate estimates of the linear growth rate of structure,  $f$ , the clustering amplitude,  $\sigma_8$ , and some of the parameters entering the galaxy biasing relation. This work, in particular, expands upon the 3PCF analysis performed by Moresco et al. (2017) on the VIPERS PDR1 by (1) using the final, larger PDR2 release; (2) exploring all triangle configurations, rather than just a subset; (3) combining two- and three-point statistics to obtain joint cosmological constraints. It is also complementary to Cappi et al. (2015) and Di Porto et al. (2016),

where the non-linearity and evolution of galaxy bias in VIPERS were first studied.

The layout of this paper is as follows. In Section 2, we briefly describe the VIPERS PDR2 catalogue and the mock data used to estimate errors. In Section 3, we describe the 2PCF and 3PCF estimators and perform validation tests using the mock samples. Covariance matrices and their estimates are discussed in Section 4. In Section 5, we present the 2PCF and 3PCF models used for the likelihood analysis of Section 6. The results of the 2PCF, the 3PCF, and their joint analyses are presented in Section 7. Finally, we discuss the results and draw our conclusions in Section 8.

Throughout the work, unless otherwise specified, we assume a flat  $\Lambda$  cold dark matter ( $\Lambda$ CDM) cosmological model characterized by the following parameters:  $\{\Omega_M, \Omega_b, n_s\} = (0.3, 0.045, 0.96)$ , as in similar VIPERS clustering works (de la Torre et al. 2017; Pezzotta et al. 2017). The Hubble constant is defined as  $H_0 = 100 h \text{ km s}^{-1} \text{ Mpc}^{-1}$ .

## 2 DATA SETS

### 2.1 VIPERS data

The VIMOS Public Extragalactic Redshift Survey (VIPERS) has been completed as one of the ESO Large Programmes. It was designed to build a spectroscopic sample of about 100 000 galaxies, aiming at an optimal combination of depth (reaching beyond  $z \simeq 1$ ), volume, and sampling density (Guzzo et al. 2014). This is obtained covering  $\sim 24 \text{ deg}^2$  over the W1 and W4 fields of the Canada–France–Hawaii Telescope Legacy Survey, which provides accurate photometry in five bands. This area was tiled with a mosaic of 288 pointings with the Visible Multi-Object Spectrograph (VIMOS) at the ESO Very Large Telescope (VLT), measuring moderate-resolution spectra ( $R \simeq 220$ ) for galaxies brighter than  $i_{AB} = 22.5$ . A colour pre-selection in the  $(r - i)$  versus  $(u - g)$  plane was applied prior to the spectroscopic observations, efficiently and accurately excluding objects with  $z < 0.5$ , and boosting the spectroscopic sampling to nearly 50 per cent. The root mean square (rms) redshift measurement error of these data is  $\sigma_z = 5 \times 10^{-4}(1 + z)$ , corresponding to  $167 \text{ km s}^{-1}$ . For consistency with previous clustering analyses of the VIPERS data, we only consider objects with a redshift confirmation rate larger than 96.1 per cent, corresponding to quality flags from 2 to 9. More details on the survey design and the final data release can be found in Guzzo et al. (2014) and Scodreggio et al. (2018), respectively.

For the work presented here, we extract from the PDR2 catalogue four different subsamples, whose characteristics are summarized in Table 1. The samples P1 and P2 are magnitude-limited samples corresponding to two redshift bins,  $z = [0.5, 0.7]$  and  $[0.7, 1.2]$ , following the selection criteria used in Pezzotta et al. (2017). They will be used to validate our analysis against previous measurements from the same data. This selection maximizes the number of available tracers, at the price of a redshift-dependent selection function and a mean density and bias that vary with redshift, especially in the outer redshift bin, which reaches  $z = 1.2$  with a rather sparse bright population.

The samples named G1 and G2 are those used for the specific new analyses of this paper. They are two volume-limited, non-overlapping bins at  $z = [0.5, 0.7]$  and  $z = [0.7, 0.9]$ , coinciding with the samples named L1 and L3 in the subhalo abundance matching (SHAM) analysis of PDR2 by Granett et al. (2019; see also Davidzon et al. 2016). The absolute magnitude thresholds guarantee completeness above 90 per cent, while evolution (both in luminosity and bias) is

**Table 1.** Definition of the subsamples of the VIPERS PDR2 catalogue that we have considered in this work. P1 and P2 are magnitude-limited samples that match those analysed in Pezzotta et al. (2017) and are used here for validation and consistency tests. G1 and G2 are instead volume-limited samples, upon which the joint clustering analysis specific of this work is based.

Name	$z$ range	Mean $z$	Magnitude cut	Number of objects
G1	$0.5 \leq z < 0.7$	0.61	$M_B < -19.3 + (0.7 - z)$	23 352
G2	$0.7 \leq z < 0.9$	0.8	$M_B < -20.3 + (0.9 - z)$	13 046
P1	$0.5 \leq z < 0.7$	0.61	$i_{AB} \leq 22.5$	30 764
P2	$0.7 \leq z < 1.2$	0.87	$i_{AB} \leq 22.5$	35 734

minimized by the limited redshift size of the bins. Galaxies within G1 and G2 are brighter on average than those in P1 and P2. As a consequence, the measured clustering amplitude is expected to be larger due to the higher galaxy bias (Marulli et al. 2013), hence partly compensating for the larger Poisson noise.

## 2.2 Weights

The completeness of the spectroscopic sample is quantified in the PDR2 catalogue by a direction-dependent target sampling rate (TSR) and a spectroscopic success rate (SSR; Scodreggio et al. 2018). To account for these, we have used the same weighting scheme as in Pezzotta et al. (2017). To each object, a statistical weight  $w_i$  is assigned as

$$w_i = w_i^{\text{TSR}} w_i^{\text{SSR}}. \quad (1)$$

Here,  $w_i^{\text{TSR}}$  is defined as the ratio of the local surface densities of target and parent galaxies (i.e. before and after applying the target selection) within an aperture of  $60 \times 100 \text{ arcsec}^2$ .  $w_i^{\text{SSR}}$  is instead the local fraction of observed spectra with reliable redshift measurement with respect to the target sample. We also correct for the small-scale bias introduced by slit ‘collisions’ by up-weighting each galaxy–galaxy pair at a given angular separation according to de la Torre et al. (2013). On the scales of our analysis, this last correction impacts the estimated 2PCF quadrupole moment, but not the monopole. We refer the interested reader to section 4 of Pezzotta et al. (2017) for further details on the weighting scheme.

## 2.3 Mock VIPERS data

To validate our analysis and quantify statistical errors, we use the publicly available VIPERS mock catalogues.<sup>1</sup> These were generated from light-cones extracted from the Big MultiDark  $N$ -body simulation (Klypin et al. 2016). The cosmology of that simulations is a flat  $\Lambda$ CDM characterized by the set of parameters  $(\Omega_M, \Omega_\Lambda, \Omega_b, h, n_s, \sigma_8) = (0.307, 0.693, 0.0482, 0.678, 0.960, 0.823)$ , which are slightly different from those used in this work. Dark matter haloes were identified in the parent simulation and populated with synthetic galaxies down to the faint magnitude limit of the survey, as detailed in de la Torre et al. (2013, 2017). This resulted in 153 independent mock VIPERS W1+W4 catalogues, on which the same footprint and selection function of the real survey were applied. These mocks were designed to match the luminosity function, number density, and redshift distribution of VIPERS galaxies. Previous analyses have shown that they also reproduce the VIPERS 2PCF (Granett et al. 2019). We will see in Section 3.2 that, within the errors, they also match the 3PCF of VIPERS galaxies.

<sup>1</sup>The VIPERS mock catalogues are publicly available at <http://www.vipers.naf.it/rel-pdr2.html#mocks>

For each mock catalogue, four subsamples corresponding to the G1, G2, P1, and P2 selections of Table 1 were created.

## 3 CLUSTERING MEASUREMENTS

The estimators used in this work belong to the class of unbiased, minimum variance  $N$ -point estimators proposed by Szapudi & Szalay (1998). Their general form is

$$\xi^N = \frac{(D - R)^N}{R^N}, \quad (2)$$

where  $D$  is the data catalogue,  $R$  is the so-called ‘random’ sample, and  $N$  is the order of the correlation statistics. The estimate relies on counting and binning all  $N$ -tuples  $D^q R^p$  formed by  $q$  data and  $p$  random objects, with  $q + p = N$ .

The ‘random’ catalogue of objects is a synthetic sample with the same geometry and selection function as the real survey but with no spatial clustering. We assume that the selection function, i.e. the probability to observe a galaxy at the spatial position  $(\alpha, \delta, z)$ , can be factorized as

$$P(\alpha, \delta, z) = f(\alpha, \delta)N(z), \quad (3)$$

where  $f(\alpha, \delta)$  accounts for the angular footprint of the survey and  $N(z)$  is the redshift distribution of the sources in the catalogue.

All measurements presented here have been performed using the estimators described below and publicly available in the library CosmoBolognaLib<sup>2</sup> (Marulli, Veropalumbo & Moresco 2016).

### 3.1 2PCF estimator

To estimate the anisotropic 2PCF we use the Landy & Szalay (1993) estimator:

$$\xi(s, \mu) = \frac{DD(s, \mu) - 2DR(s, \mu) + RR(s, \mu)}{RR(s, \mu)}, \quad (4)$$

where  $DD$ ,  $DR$ , and  $RR$  are the data–data, data–random, and random–random pairs of objects, respectively. The separation vector of two objects has modulus  $s$  and forms a cosine angle  $\mu = \cos(\theta)$  with the line of sight to the pair, measured at the mid-point of the separation vector itself.

We bin the pair counts using a constant logarithmic bin in  $s$ ,  $\Delta \log(s) = 0.1$ , and a linear one for  $\mu$ ,  $\Delta \mu = 0.05$ , as in Pezzotta et al. (2017).

For each  $s$  bin we compute the 2PCF multipoles:

$$\xi_l(s) = \frac{2l + 1}{2} \int_{-1}^1 d\mu \mathcal{P}_l(\mu) \xi(s, \mu), \quad (5)$$

where  $\mathcal{P}_l(\mu)$  are the Legendre polynomials. We only consider the monopole  $\ell = 0$  and quadrupole  $\ell = 2$ , since odd multipoles are zero

<sup>2</sup><https://gitlab.com/federicomarulli/CosmoBolognaLib>

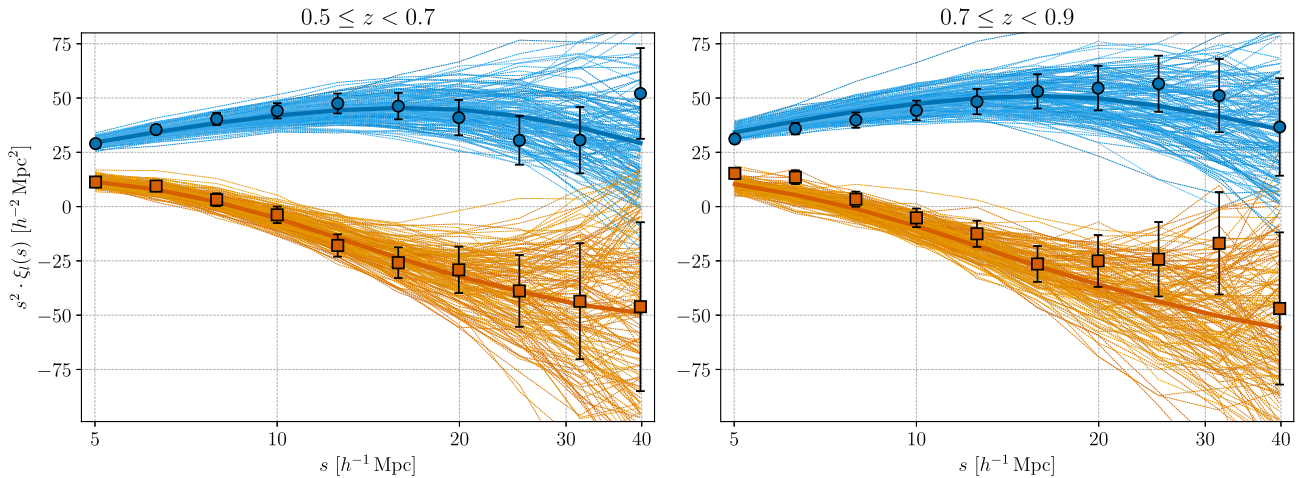


**Figure 1.** Monopole (blue circles) and quadrupole (orange squares) moments of the 2PCF measured from the G1 (left) and G2 (right) VIPERS subsamples. The corresponding measurements from the 153 VIPERS mock catalogues are also plotted (thin solid lines), together with their average (thick solid line). The error bars on the data points correspond to the rms dispersion of the mocks. The consistency between the mocks and the real data highlights the very good fidelity in clustering properties of the mock galaxies.

by design, and the measured hexadecapole turns out to be consistent with zero within the (large) errors.

To validate our estimator, we measure the 2PCF multipoles for the subsamples of Table 1 and compare the results with those of previous VIPERS studies. Fig. 1 shows the 2PCF monopole and quadrupole moments of the VIPERS G1 and G2 samples (blue circles and the orange squares, respectively). The solid thin lines correspond to measurements of each mock catalogue, with the thicker line and error bars on data points showing the average and rms of the mocks, respectively. This plot shows how the mock VIPERS samples reproduce faithfully the clustering of the real data, suggesting that they are adequate to estimate their errors and covariance. We have repeated the test using the P1 and P2 samples and verified that the results match those of Pezzotta et al. (2017, see fig. 12). We notice a mismatch between real data and mocks at small separations ( $< 7 h^{-1}$  Mpc) in G2 sample. A similar effect is also seen in the Pezzotta et al. (2017) analysis (though on a wider redshift range, see bottom panel of their fig. 8). This mismatch may point to some systematic, small-scale effects in the procedure that generates the mock galaxies. This effect, however, does not impact our results, as we will perform the analysis using larger scales (see discussion in Section 7.1).

The maximum separation considered in our analysis is set by the signal-to-noise ratio of the 2PCF. The VIPERS footprint is highly elongated along the (equatorial) longitude, which significantly reduces the number of distant pairs in the transverse direction. As a result, the estimated quadrupole moment becomes noisy beyond  $\sim 40 h^{-1}$  Mpc. We therefore set  $s_{\max} = 40 h^{-1}$  Mpc in our 2PCF analysis. In Section 7.1, we will also test the sensitivity of the results to the smallest separation scale considered, showing that the results are robust down to  $s_{\min} = 15 h^{-1}$  Mpc, which we then assume as the default value. In summary, our baseline range for the 2PCF analysis is  $[15, 40] h^{-1}$  Mpc.

### 3.2 3PCF estimator

To measure the 3PCF of the VIPERS first data release catalogue (PDR1), Moresco et al. (2017) used the estimator of Szapudi & Szalay (1998) because of its ability to account for complicated survey geometry (Kayo et al. 2004). This estimator, however, is

computationally demanding since it relies on brute-force galaxy triplet counting, whose computing time-scales as  $O(N^3)$ . This becomes unbearable if applied to 153 mock catalogues with the size of VIPERS.

A major breakthrough in this respect has been the introduction by Slepian & Eisenstein (2015), of a more efficient estimator based on a spherical harmonics decomposition (SHD). For this algorithm, the computational cost scales as  $O(N^2)$ , making it successfully applicable to large galaxy samples such as the SDSS Data Release 12 (DR12) CMASS catalogue (Slepian et al. 2017b). The method relies on the 3PCF Legendre polynomials expansion proposed by Szapudi (2004):

$$\zeta(s_{12}, s_{13}, \mu) = \sum_{l=0}^{l_{\max}} \zeta_l(s_{12}, s_{13}) P_l(\mu), \quad (6)$$

where the 3PCF  $\zeta(s_{12}, s_{13}, \mu)$  is parametrized by two triangle sides  $s_{12}$ ,  $s_{13}$  and their cosine angle  $\mu = \cos(\hat{s}_{12} \cdot \hat{s}_{13})$ . This expansion offers two advantages. The first one is that the multipole moments  $\zeta_l(s_{12}, s_{13})$  can be efficiently estimated by locally expanding the density field at distances  $s_{12}$  and  $s_{13}$  in spherical harmonics and then by cross-correlating the expansion coefficients using the spherical harmonics addition theorem. The second advantage is that equation (6) typically requires a limited number of multipoles to converge. These properties dramatically reduce the computational cost, allowing us to measure the 3PCF in all VIPERS mocks and consider all triangle configurations. We refer the reader to Slepian & Eisenstein (2015) for a detailed description of the SHD estimator.

The main disadvantages of this estimator are that, for a given configuration, all triangles are mixed together; this is particularly relevant in all cases where the third side spans a large range of scales. For example, in the case of isosceles configurations with  $s_{12} = s_{13}$ , the third side  $s_{23}$  varies from 0 to  $2 \times s_{12}$ , i.e. well into the highly non-linear regime, where theoretical predictions cannot be trusted. For this reason, here we will only consider triangles with all side lengths above a minimum value  $s_{\min} = 15 h^{-1}$  Mpc and up to a maximum length  $s_{\max} = 40 h^{-1}$  Mpc. This matches the scale used in the 2PCF analysis. In Section 7.2, we shall test the robustness of our results to such a choice.

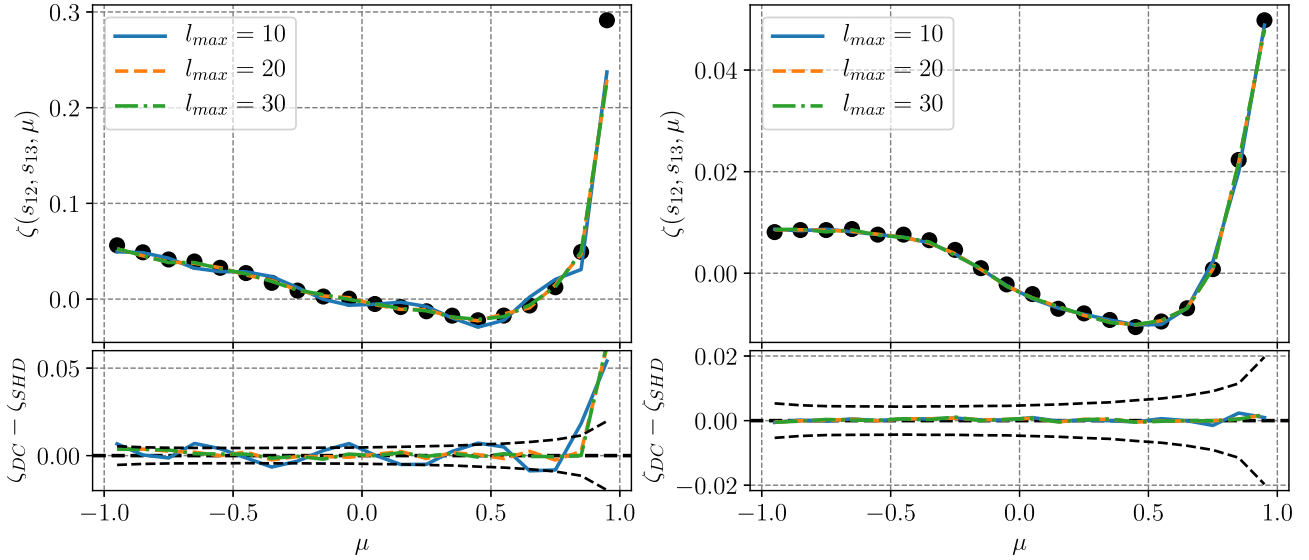


**Figure 2.** Top panels: estimates of the three-point correlation function (3PCF) for the G1 sample using both the triplet counting method (black dots) and the SHD method (solid lines), for different  $l_{\max}$  as indicated by the legend (top panels). The left- and right-hand panels correspond to isosceles ( $s_{12} = s_{13} = 15 h^{-1}$  Mpc) and non-isosceles ( $s_{12} = 15 h^{-1}$  Mpc,  $s_{13} = 30 h^{-1}$  Mpc) configurations, respectively. The bottom panels show the difference between the two estimators, for the different choices of  $l_{\max}$  (blue solid, orange dashed, and green dot-dashed lines). The dashed black curves correspond to  $\pm 10$  per cent of the statistical scatter of the mocks, highlighting the relative importance of the systematic errors introduced by the choice of  $l_{\max}$ .

### 3.2.1 Convergence of the SHD method

We first assess the sensitivity of the SHD method to the choice of  $l_{\max}$  in equation (6). We thus compare the 3PCF of the G1 catalogue measured with the SHD method to that, supposedly exact, estimated with the same brute-force triplet counting technique used by Moresco et al. (2017). We show in Fig. 2 the results for two triangle configurations: isosceles triangles with  $s_{12} = s_{13} = 15 h^{-1}$  Mpc (left-hand panel) and non-isosceles triangles with  $s_{12} = 15 h^{-1}$  Mpc and  $s_{13} = 30 h^{-1}$  Mpc (right-hand panel). In both cases, the same  $\mu$  binning is used. We expect similar results for different choices of  $s_{12}, s_{13}$ .

In the top panels, we compare the reference 3PCF measured with the triplet counting technique (black dots), with the one measured with the SHD method using  $l_{\max} = 10, 20$ , and  $30$  (lines with different colours). These particular choices of configurations cover both the cases where highly non-linear scales are included (isosceles, left-hand panel) or not (non-isosceles, right-hand panel). In the bottom panels, we show the difference of the 3PCFs estimated with the two methods. As an indication of the relative value of the potential systematic error with respect to statistical errors, the black dashed lines indicate 10 per cent of the rms scatter among the mock catalogues. For non-isosceles configurations (right-hand panel), the SHD matches well the expected result, with differences of the order (or below) 1 per cent of the random errors, almost independently of the choice of  $l_{\max}$ . This implies that a limited number of multipoles  $\ell$  are sufficient for equation (6) to converge to the correct result, typically  $l < 10$ .

On the contrary, the results of the SHD method for the isosceles configurations (left-hand panel) depend on the choice of  $l_{\max}$  and  $\mu$ . For  $l_{\max} = 30$ , the results are generally satisfactory (the difference between SHD and triplet counting is of the order of a few per cent of the statistical error), except for  $\mu = 1$ , i.e. when  $s_{23} \rightarrow 0$ . This is not surprising, since elongated isosceles triangle shapes are difficult to reproduce in harmonics space.

Based on these results, we adopt a conservative approach in which (1) we set  $l_{\max} = 30$  in the 3PCF estimate, and (2) we exclude the case

$\mu = 1$  for isosceles configurations. We also choose to parametrize the 3PCF in terms of the three side lengths  $\zeta(s_{12}, s_{13}, s_{23})$  instead of two sides and the cosine angle,  $\zeta(s_{12}, s_{13}, \mu)$ . Since the SHD method involves binning in the radial direction, we perform an additional step, described in Appendix A, to use the same binning along the three sides  $s_{12}, s_{13}$ , and  $s_{23}$ .

Finally, we sort the triangles in increasing size  $s_{12} \leq s_{13} \leq s_{23}$ , to avoid repetitions. This choice also facilitates triangle selection: for example, we can exclude scales smaller than a chosen value by setting a threshold for one triangle side only.

### 3.2.2 Comparison with the 3PCF of mock samples

The second test is analogous to the one performed to validate the 2PCF estimator: we measure the 3PCF in the G1, G2, P1, and P2 VIPERS samples and compare the results with the same quantity measured in the mocks.

In Fig. 3, we show the results for the G1 and G2 samples (top and bottom panels, respectively). We detect a non-zero 3PCF signal up to the largest scales considered in our analysis, in agreement with Moresco et al. (2017). The VIPERS 3PCF agrees well with that of the mock samples, demonstrating that the VIPERS mocks are indeed adequate to estimate the errors for the 3PCF analysis, too. We notice a mismatch for the sample G1 on large triangles. This may indicate the presence of observational systematic effects not fully accounted for. However, we stress that the significance of this mismatch should not be overemphasized, given the strong covariance among the 3PCF measurements in nearby bins. For this reason we will still include these triangles for the analysis.

## 4 COVARIANT ERRORS

To estimate the errors, we will not adopt an analytic, Gaussian model (like in e.g. Slepian & Eisenstein 2017). Instead, supported by the results of the previous section, we directly estimate errors and their

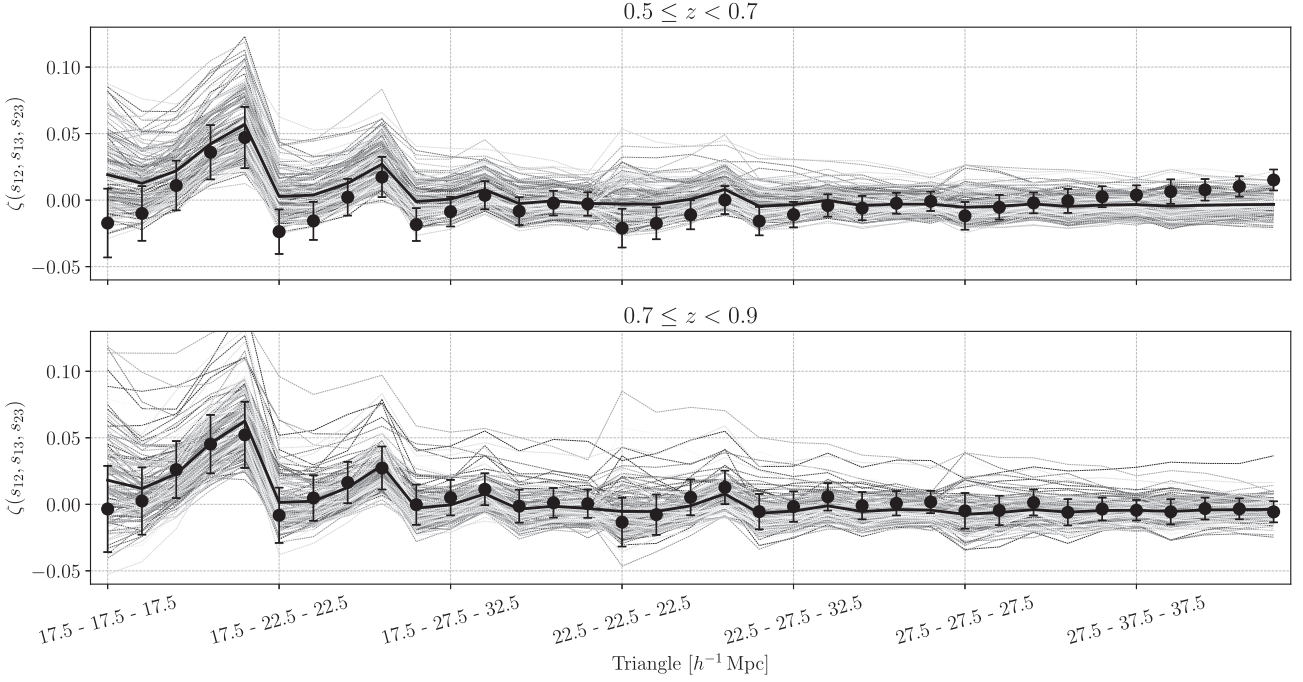


**Figure 3.** Monopole moments (black circles) of the three-point correlation function (3PCF) for the G1 and G2 samples (top and bottom panels, respectively), measured for some selected sets of triangles of different side lengths, as indicated on the x-axis. The corresponding measurements from the 153 VIPERS mock catalogues are also shown by the thin grey lines, together with their averages (solid black line). Error bars correspond to the rms scatter among the mocks.

covariance matrix  $C_{i,j}$  from the mock VIPERS catalogues, as

$$C_{i,j} = \frac{1}{N_m - 1} \sum_{k=0}^{N_m} (d_i^k - \bar{d}_i) (d_j^k - \bar{d}_j), \quad (7)$$

where  $d_i^k$  indicates the data vector in the  $i$ th bin and in the  $k$ th mock catalogue. The size of the data vector and of the covariance matrix depends on the specific clustering analysis being performed. In the 2PCF analysis, performed in the range  $15 \leq s_{\min}^{\text{2pt}} \leq 40 h^{-1}$  Mpc, the size of the data vector is 10 and the corresponding  $10 \times 10$  covariance matrix is shown in the lower left-hand part of Fig. 4. For the 3PCF analysis, performed over the same range of scales, the size of the data vector is 35 and the covariance matrix corresponds to the upper-right-hand part of the same figure. In the joint 2PCF and 3PCF analysis, the data vector has 45 elements and the covariance matrix, which also contains the 2PCF–3PCF cross-terms, corresponds to the full matrix of Fig. 4.

Both precision and accuracy of our covariance matrix depend on the number of mock catalogues used for its numerical estimation. Since this number is limited, a correction for the expected systematic errors should be considered (see e.g. discussion in Hartlap, Simon & Schneider 2007; Percival et al. 2014). To this end, we follow Sellentin & Heavens (2016) in using a modified likelihood function, which we discuss in detail in Section 6.

## 5 MODELLING THE GALAXY 2- AND 3-POINT CORRELATION FUNCTIONS

In this section, we describe our model for the anisotropic galaxy 2PCF,

$$\xi_g(s, \mu) = \langle \delta_g(\mathbf{x}) \delta_g(\mathbf{x} + \mathbf{s}) \rangle, \quad (8)$$

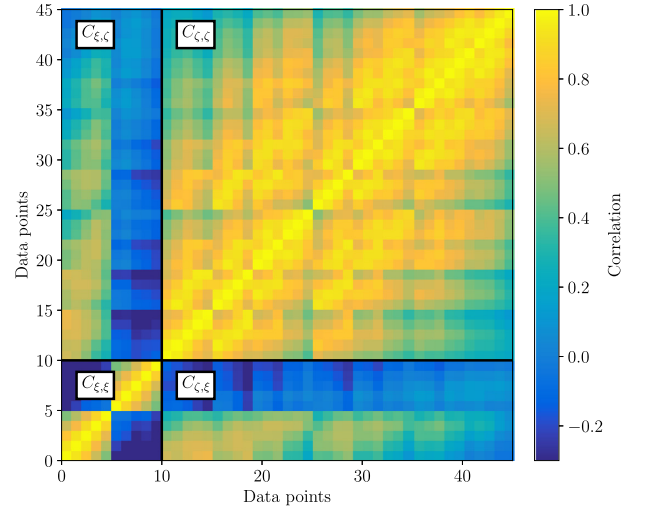


**Figure 4.** The global correlation matrix used in our joint likelihood analysis of the 2PCF and 3PCF, estimated from the 153 VIPERS mock catalogues using equation (7). We show here the one for the G1 sample, as an illustrative example. The matrix is composed of two subblocks, corresponding to the 2PCF monopole and quadrupole ( $C_{\xi,\xi}$ , bottom left), and the 3PCF monopole ( $C_{\zeta,\zeta}$ , top right), respectively, together with their cross-covariance ( $C_{\xi,\zeta}$ ). The subarrays are used for the separate 2PCF and 3PCF analyses, while the full  $45 \times 45$  matrix is used in the joint likelihood analysis.

and 3PCF,

$$\zeta_g(s_{12}, s_{13}, s_{23}) = \langle \delta_g(\mathbf{x}) \delta_g(\mathbf{x} + \mathbf{s}_{12}) \delta_g(\mathbf{x} + \mathbf{s}_{13}) \rangle. \quad (9)$$

In these expressions,  $\delta_g(\mathbf{x})$  is the galaxy density contrast at the position  $\mathbf{x}$ , while  $\langle \dots \rangle$  indicates ensemble average.

The model relies on the approach of Scoccimarro, Zaldarriaga & Hui (1999), Scoccimarro (2004), McDonald & Roy (2009), Saito

et al. (2014), and has already been used to perform 2PCF, 3PCF, and joint 2PCF+3PCF analyses (Gil-Marín et al. 2015; de la Torre et al. 2017; Slepian & Eisenstein 2017).

### 5.1 Galaxy bias

The first ingredient of the model is the galaxy biasing relation of McDonald & Roy (2009):

$$\delta_g = b_1 \delta + \frac{b_2}{2} [\delta^2 - \langle \delta^2 \rangle] + \frac{b_{s^2}}{2} [s^2 - \langle s^2 \rangle] + O(\delta^3). \quad (10)$$

In this expression, the galaxy density contrast  $\delta_g$  is a function of the matter non-linear overdensity  $\delta$  and of the non-local tidal field  $s^2$ , which accounts for dependence of  $\delta_g$  on the local potential  $\phi$  (see e.g. section II of McDonald & Roy 2009). The terms  $\langle \delta^2 \rangle$  and  $\langle s^2 \rangle$  guarantee that  $\langle \delta_g \rangle = 0$ . This bias model is then characterized by the four parameters  $b_1$ ,  $b_2$ ,  $b_{s^2}$ , and  $b_{3nl}$ .

### 5.2 Distortion effects

Using the observed spectroscopic redshifts as a distance proxy introduces spurious distortions in the clustering properties that need to be accounted for. Three types of distortions need to be considered: those introduced by the departures from the Hubble flow; those induced by assuming an incorrect cosmological model in computing distances from redshifts; and those due to the errors on the measured redshifts.

#### 5.2.1 Peculiar motions

Peculiar velocities introduce a Doppler shift that modifies the mapping between spatial positions,  $\mathbf{x}$ , and the measured positions,  $\mathbf{s}$ :

$$\mathbf{s} = \mathbf{x} + \frac{v_{\parallel}}{aH(a)} \mathbf{e}_{\parallel}, \quad (11)$$

where  $a$  is the expansion factor,  $v_{\parallel}$  is the radial component of the peculiar velocity vector,  $\mathbf{e}_{\parallel}$  is the unit radial vector, and  $\mathbf{s}$  is the redshift-space vector position of the object.

This mapping introduces a relation between the measured (redshift-space) galaxy overdensity,  $\delta_g(\mathbf{s})$ , and the true, real-space one,  $\delta_g(\mathbf{x})$ :

$$\delta_g(\mathbf{s}) = [1 + \delta_g(\mathbf{x})] \left| \frac{d^3 s}{d^3 x} \right|^{-1} - 1, \quad (12)$$

where  $\left| \frac{d^3 s}{d^3 x} \right|^{-1}$  is the Jacobian of the map in equation (11).

In this work, we make the plane-parallel hypothesis, i.e. we assume that the relative separations between galaxy pairs are much smaller than the distance to the observer. This assumption is fully justified, since the maximum scale considered in our analyses ( $40 h^{-1}$  Mpc) is much smaller than any distance to a VIPERS galaxy, which lies at  $z \geq 0.5$ . Under this approximation, equation (12) becomes

$$\delta_g(\mathbf{s}) = \frac{\delta_g(\mathbf{x}) + f \partial_{\parallel} \mathbf{u}}{1 - f \partial_{\parallel} \mathbf{u}}, \quad (13)$$

where the partial derivative is taken along the radial direction,  $\mathbf{u}$  is the peculiar velocity, and  $f$  is the linear growth rate of density fluctuations,

$$f = \frac{d \log D}{d \log a} \approx \Omega_M^{0.545}(z), \quad (14)$$

where  $D(z)$  is the linear growth factor and the second relation is a good approximation in the flat  $\Lambda$ CDM model assumed here (see e.g. Wang & Steinhardt 1998; Huterer & Linder 2007).

#### 5.2.2 Geometrical distortions

Choosing an incorrect fiducial cosmology to estimate distances from redshifts generates another kind of anisotropy, the well-known Alcock–Paczynski effect (Alcock & Paczynski 1979). The detection of this effect on intrinsically isotropic clustering features as the BAO peak in the 2PCF has been used to trace the expansion history of the Universe (Eisenstein et al. 2005; Kazin et al. 2013). Here, we will treat this effect as a nuisance to be marginalized over, since our analysis is limited to scales well below the BAO peak. As shown in de la Torre et al. (2017), the impact of this marginalization in the error budget of the VIPERS clustering analysis is negligible. Therefore, we will set our fiducial cosmology equal to the flat  $\Lambda$ CDM model specified in Section 1 and safely ignore the Alcock–Paczynski effect.

#### 5.2.3 Redshift measurement errors

Redshift measurement errors introduce a noise in the redshift-to-distance relation analogous to that of incoherent motions (Marulli et al. 2012), effectively erasing information on scales below:

$$\sigma_{\pi} = \frac{c \sigma_z}{H(z)} h^{-1} \text{ Mpc}, \quad (15)$$

where  $\sigma_z$  is the rms error typical of the adopted instrumental setup. For VIPERS, the errors are very well described by a Gaussian distribution with  $\sigma_z = 5 \times 10^{-4}(1+z)$ , corresponding to a length scale  $\sigma_{\pi} \sim 1.5 h^{-1}$  Mpc (Sereni et al. 2015; Scodreggio et al. 2018).

### 5.3 2PCF model

To model the galaxy 2PCF we start from the matter power spectrum  $P(k)$ ,

$$\langle \delta(\mathbf{k}) \delta(\mathbf{k}') \rangle = 2\pi^3 \delta_D(\mathbf{k} - \mathbf{k}') P(|\mathbf{k}|). \quad (16)$$

Using equation (13) to account for RSDs, we obtain an expression of the redshift-space power spectrum:

$$P^s(k, v) = \int d^3 \mathbf{r} e^{-i\mathbf{k} \cdot \mathbf{r}} \langle e^{-ifk\nu\Delta u_{\parallel}} \times [\delta(\mathbf{x}) + f \partial_{\parallel} u_{\parallel}(\mathbf{x})] [\delta(\mathbf{x}') + f \partial_{\parallel} u_{\parallel}(\mathbf{x}')] \rangle, \quad (17)$$

where  $\nu = k_{\parallel}/k$ ,  $u_{\parallel} = -v_{\parallel}/(faH(a))$ ,  $v_{\parallel}$  and  $k_{\parallel}$  are the radial components of the peculiar velocity and wavenumber vectors, respectively,  $\delta$  is the matter overdensity,  $u_{\parallel} = u_{\parallel}(\mathbf{x}) - u_{\parallel}(\mathbf{x}')$ , and  $\mathbf{r} = \mathbf{x} - \mathbf{x}'$ . The term in square brackets accounts for the effect of coherent motions that increase the clustering amplitude, whereas the exponential factor encodes the ‘Fingers of God’ effect of incoherent motions. For a more detailed description, see Taruya, Nishimichi & Saito (2010).

Equation (17) is exact but of impractical use. Rather, using the approximations introduced by Scoccimarro (2004) and Taruya et al. (2010) for the case of biased mass tracers, we obtain the simpler expression

$$P_g^s(k, v) = D(\sigma_{12}, \sigma_z) [P_{gg}(k) + 2v^2 f P_{g\theta}(k) + v^4 f^2 P_{\theta\theta}(k)], \quad (18)$$

where

$$\begin{aligned}
 P_{\text{gg}}(k) &= b_1^2 P_{\delta\delta}(k) + 2b_2 b_1 P_{b_2, \delta}(k) + 2b_{s_2} b_1 P_{b_{s_2}, \delta}(k) \\
 &+ b_2^2 P_{b_2 22}(k) + 2b_2 b_{s_2} P_{b_2 s_2}(k) + b_{s_2}^2 P_{b_{s_2} 22}(k) \\
 &+ 2b_1 b_{3\text{nl}} \sigma_3^2(k) P_{\text{lin}}(k), \quad (19)
 \end{aligned}$$

$$\begin{aligned}
 P_{\text{g}\theta}(k) &= b_1 P_{\delta\theta}(k) + b_2 P_{b_2, \theta}(k) + b_{s_2} P_{b_{s_2}, \theta}(k) \\
 &+ b_{3\text{nl}} \sigma_3^2(k) P_{\text{lin}}(k). \quad (20)
 \end{aligned}$$

In these equations,  $P_{\delta\delta}$ ,  $P_{\delta\theta}$ , and  $P_{\theta\theta}$  are, respectively, the non-linear matter density–density, density–(velocity divergence), and (velocity divergence)–(velocity divergence) power spectra.  $P_{\text{lin}}$  is the matter linear power spectrum, and  $P_{b_2, \delta}$ ,  $P_{b_{s_2}, \delta}$ ,  $P_{b_2, \theta}$ ,  $P_{b_{s_2}, \theta}$ ,  $P_{b_2 22}$ ,  $P_{b_{s_2} 22}$ ,  $P_{b_2 s_2}$ , and  $\sigma_3^2$  are one-loop bias integrals; their expressions can be found in e.g. Gil-Marín et al. (2015) and de la Torre et al. (2017). The linear and non-linear power spectra of density and velocity divergence are specified at the effective redshift of the sample. To model  $P_{\text{lin}}$  we use the CAMB Boltzmann solver code (Lewis, Challinor & Lasenby 2000; Howlett et al. 2012), whereas for  $P_{\delta\delta}(k)$ ,  $P_{\delta\theta}$ , and  $P_{\theta\theta}$  we use the standard perturbation theory (SPT) one-loop model of Scoccimarro (2004, equations 63–65). In this model, the degree of non-linearity in  $P_{\delta\delta}$ ,  $P_{\delta\theta}$ , and  $P_{\theta\theta}$  is quantified by the same parameter that measures the clustering amplitude, i.e.  $\sigma_8(z)$ .

In equation (18), we have introduced the term  $D(\sigma_{12}, \sigma_z)$  to model the combined damping effect of incoherent motions and redshift errors. Its explicit expression is

$$D(\sigma_{12}, \sigma_z) = (1 + k^2 v^2 \sigma_{12}^2)^{-1} \exp(-k^2 v^2 \sigma_z^2). \quad (21)$$

The first term, modelled as a Lorentzian damping, accounts for the effect of random motions within dark matter haloes, quantified by the pairwise velocity dispersion  $\sigma_{12}$ . The second term accounts for the redshift measurement errors and is modelled as a Gaussian function. In our analysis, we fix  $\sigma_z$  to the VIPERS estimated value and leave  $\sigma_{12}$  as a free factor we can fit for and then treat it as a nuisance parameter.

Since the 2PCF model fits well the corresponding measurements from the VIPERS mocks on all scales considered, we decided to ignore the model correction terms  $C_A(k, v, f, b_1)$  and  $C_B(k, v, f, b_1)$  of Taruya et al. (2010), which are instead considered in other analyses (e.g. Gil-Marín et al. 2015).

To test the robustness of our model, we also considered an alternative 2PCF model, in which we used (1) the HALOFIT semi-analytical prescription calibrated by Takahashi et al. (2012) to model the matter power spectra, and (2) the fitting functions of Bel et al. (2019) to model  $P_{\delta, \theta}(k)$  and  $P_{\theta, \theta}(k)$ . We find that the alternative model provides results very similar to the original one, the differences being much smaller than the statistical errors.

We then use equation (18) to model the multipole moments of the anisotropic power spectrum,

$$P_\ell^s(k) = \frac{2\ell + 1}{2} \int_{-1}^1 P_g^s(k, \nu) \mathcal{P}_\ell(\nu) d\nu, \quad (22)$$

and, from these, the multipole moments of the anisotropic 2PCF,

$$\xi_\ell^s(s) = i^\ell \int \frac{k^2}{2\pi^2} P_\ell^s(k) j_\ell(ks) dk, \quad (23)$$

where  $j_\ell$  indicates the spherical Bessel functions. Having neglected the  $C_A(k, v, f, b_1)$  terms, in our model the parameters  $b_1$  and  $f$  are fully degenerate with  $\sigma_8$ . The two bias parameters  $b_1$  and  $b_2$  are also highly degenerate.

## 5.4 3PCF model

The 3PCF model we adopt is the same one used by Slepian & Eisenstein (2017) and Slepian et al. (2017a) to detect the BAO feature in the 3PCF of SDSS DR12 galaxies and to measure their biasing relation in redshift space.

Our 3PCF model is derived from galaxy bispectrum  $B(|\mathbf{k}_1|, |\mathbf{k}_2|, |\mathbf{k}_3|)$ , defined as

$$\langle \delta_g(\mathbf{k}_1) \delta_g(\mathbf{k}_2) \delta_g(\mathbf{k}_3) \rangle = \delta_D(\mathbf{k}_1 + \mathbf{k}_2 + \mathbf{k}_3) B(|\mathbf{k}_1|, |\mathbf{k}_2|, |\mathbf{k}_3|). \quad (24)$$

In particular, we assume the redshift-space tree-level galaxy bispectrum derived in Scoccimarro et al. (1999). From this, we obtain the 3PCF model by Fourier transform, following the prescriptions of Slepian et al. (2017b).

The 3PCF model can be expressed as

$$\begin{aligned}
 \zeta(s_{12}, s_{13}, s_{23}) &= \sum_{l=0}^{l=4} A_l(b_1, \gamma, \gamma', \beta) f_l(s_{12}, s_{13}, s_{23}) \\
 &+ B(b_1, \beta) \sum_{l=0}^{l=\text{max}} k_l(s_{12}, s_{13}, s_{23}), \quad (25)
 \end{aligned}$$

where  $\gamma \equiv b_2/b_1$  and  $\gamma' \equiv b_{s_2}/b_1$  are combinations of the bias parameters. The first term of equation (25) accounts for contributions separable in  $k_1, k_2$  in the Scoccimarro et al. (1999) bispectrum model. Its Fourier transform can be computed analytically as the product of two quantities. The first one,  $A_l$ , depends on the bias parameters,  $b_1, b_2, b_{s_2}$ , and on the linear distortion parameter  $\beta = f/b_1$ . The second one,  $f_l$ , depends on the linear power spectrum,  $P_{\text{lin}}(k)$ . The explicit expression of the  $A_l$  and  $f_l$  terms is given in Appendix B.

The second term in equation (25) accounts for the non-separable terms (i.e. the terms in which  $k_3$  appears explicitly). It is also made-up of two terms. The multiplicative factor  $B = b_1^3(7\beta^2 + 2\beta^3)$  depends on  $b_1$  and  $\beta$ , while the terms  $k_l(s_{12}, s_{13}, s_{23})$  in the sum depend on  $P_{\text{lin}}(k)$ . Their explicit expressions are given in equations (17)–(19) of Slepian et al. (2017b). The contribution of non-separable terms is small compared to that of the separable one and therefore we will ignore them in the 3PCF model, similarly to what we did with the  $C_A$  and  $C_B$  terms in the 2PCF model.

Scoccimarro et al. (1999) and Gil-Marín et al. (2015) have modelled the effect of incoherent motions with a damping term in the galaxy bispectrum,

$$D^B(\alpha\sigma_{12}) = \left\{ 1 + \alpha^2 [(k_1 v_1)^2 + (k_2 v_2)^2 + (k_3 v_3)^2]^2 \frac{\sigma_{12}^2}{2} \right\}^{-2}. \quad (26)$$

The magnitude of the damping effect is determined by the pairwise velocity dispersion,  $\sigma_{12}$  and modulated, in the model, by a multiplicative factor,  $\alpha$  (with  $\alpha = 0$  describing a purely coherent flow). In this work, however, we decided to drop this damping term since it has a negligible impact on scales larger than  $10 h^{-1}$  Mpc as we show in a dedicated test in Section 7.2, where we assess the sensitivity of our results to the choice of  $s_{\text{min}}$ . This choice has the further advantage of avoiding computationally demanding two-dimensional Fourier transforms.

## 5.5 Integral constraint

The so-called integral constraint effect originates from the assumption that the mean density estimated from the data coincide with the true one. This assumption biases the estimate of the correlation function on scales comparable to the size of the survey (Hui & Gaztañaga 1999), where it cannot be neglected, in particular at BAO



**Table 2.** Priors for the free parameters used in our likelihood analyses. The pairwise velocity dispersion,  $\sigma_{12}$ , is expressed in  $h^{-1}$  Mpc.

Analysis/Parameters	$b_1$	$\gamma$	$\beta$	$\sigma_8(z)$	$\sigma_{12}$
2PCF	[0.1, 5]	[-5, 5]	[0.1, 5]	[0, 5]	[0, 10]
3PCF	[0.1, 5]	[-5, 5]	[0.1, 5]	[0.1, 5]	–
2PCF+3PCF	[0.1, 5]	[-5, 5]	[0.1, 5]	[0, 5]	[0, 10]

scales (Slepian & Eisenstein 2017). However, the maximum scales considered in our analysis ( $40 h^{-1}$  Mpc) are significantly smaller than the size of the survey. This guarantees that the integral constraint is negligible, as shown by Cappi et al. (2015), and will be ignored in our analysis.

### 5.6 Summary of model parameters

Our 2PCF and 3PCF models are specified by the set of free parameters listed in Table 2. These include the clustering rms amplitude,  $\sigma_8$ , the linear redshift distortion parameter  $\beta \equiv f\bar{b}_1$ , the pairwise velocity dispersion,  $\sigma_{12}$ , and the two galaxy bias parameters,  $b_1$  and  $\gamma \equiv b_2/b_1$ .

The other model parameters that are kept fixed to their fiducial values are: the shape parameters of  $P_{\text{lin}}(k)$ , which are set to the *Planck* values (Planck Collaboration VI 2020); the VIPERS rms redshift error,  $\sigma_z = 5 \times 10^{-4}(1+z)$ ; the bias parameters  $b_{s,2}$  and  $b_{3\text{nl}}$ , which are derived from local Lagrangian theory, i.e.

$$b_{s,2} = -\frac{4}{7}(b_1 - 1), \quad (27)$$

$$b_{3\text{nl}} = \frac{32}{325}(b_1 - 1). \quad (28)$$

This choice is motivated by the fact that their measured values would be too noisy, as we have verified by running a dedicated likelihood analysis, aimed at testing the local Lagrangian bias hypothesis. Finally, we set  $\alpha = 0$ ; a choice that has a negligible impact on the results, as we show in Section 7.2.

## 6 PARAMETER INFERENCE

To estimate the free parameters of the model, described as a vector  $\theta$ , and their uncertainties, we compute the posterior probability,  $P(\mu(\theta)|d)$ , where  $\mu(\theta)$  is the model prediction vector and  $d$  is the data vector.

We perform three different analyses: one in which the data vector is represented by the VIPERS 2PCF monopole and quadrupole measured in the two samples G1 and G2 in the range  $[15, 40] h^{-1}$  Mpc; one where we consider the measured 3PCF monopole of the same galaxies in the same range of scales; and one considering both statistics. In each case, we use the corresponding numerical covariance matrix  $C$  as described in Section 4.

To evaluate the posterior probability, we multiply the likelihood,  $\mathcal{L}(d|\mu, C)$ , by the prior probability,  $P(\theta)$ . For each free parameter, the prior is modelled as a step function with zero value outside the ranges specified in Table 2. To compute the likelihood  $\mathcal{L}(d|\mu, C)$ , we use the covariance matrices described in Section 4. The latter have been numerically estimated from a large (153) but finite number of mock VIPERS catalogues, which introduce a systematic error. To correct for this, we adopt the approach of Sellentin & Heavens (2016) and use the modified likelihood function:

$$\mathcal{L}(d|\mu, C, N_m) = \bar{c}_p (\det C)^{-1/2} \left[ 1 + \frac{\chi^2(\mu, C)}{N_m - 1} \right]^{-\frac{N_m}{2}}, \quad (29)$$

where

$$\chi^2(\mu, C) = (d - \mu)^T C^{-1} (d - \mu), \quad (30)$$

$$\bar{c}_p = \frac{\Gamma\left(\frac{N_m}{2}\right)}{\pi(N_m - 1)^{p/2} \Gamma\left(\frac{N_m - \ell}{2}\right)}, \quad (31)$$

with  $N_m$  being the number of mock catalogues, and  $\Gamma$  the Gamma function.

To sample the posterior  $P(\mu(\theta)|d)$  we use a Markov chain Monte Carlo (MCMC) approach that generates a set of chains, i.e. collections of points in the parameter space  $\{\theta_1, \theta_2, \dots, \theta_N\}$ . Some of the parameters used in our analysis are expected to be (partly) degenerate. In these cases, we do not consider the individual parameters, but a suitable combination, as e.g. for  $b_1\sigma_8$  and  $f\sigma_8$  in the case of the 2PCF analysis alone.

## 7 RESULTS

In this section, we present the results of three analyses based, respectively, on the VIPERS 2PCF only, 3PCF only, and on the combination of the two statistics.

The first analysis is very similar to those of de la Torre et al. (2013, 2017), Pezzotta et al. (2017), and Mohammad et al. (2018) and we use it to validate our likelihood pipeline. The main goal of the second analysis, which builds upon the work of Moresco et al. (2017), is to measure the bias parameters  $b_1$  and  $\gamma \equiv b_2/b_1$ . Finally, the joint 2PCF and 3PCF analysis is aimed at breaking parameter degeneracies to obtain independent constraints on the galaxy bias, the evolution of cosmic structures, and the clustering amplitude.

For all such analyses, the G1 and G2 VIPERS subsamples are used (see Table 1). For the 2PCF study only, we also consider the P1 and P2 samples to allow us a direct comparison to Pezzotta et al. (2017).

### 7.1 2PCF

The results of the 2PCF analysis are shown in Fig. 5. In the panels we plot the 2D and 1D posterior probability distributions for the combinations of degenerate parameters  $f\sigma_8$ ,  $b_1\sigma_8$ , and for  $\sigma_{12}$ , obtained from the analysis of the VIPERS P1 ( $\bar{z} = 0.61$ ) and P2 ( $\bar{z} = 0.87$ ) samples and for different  $s_{\text{min}}$  values indicated in the plots. We considered the 2PCF monopole and quadrupole moments and used the  $10 \times 10$  covariance submatrix  $C_{\xi, \xi}$  of Fig. 4.

Our analysis is very similar, though not identical, to that of Pezzotta et al. (2017). To minimize the differences, we compare our results obtained by using an SPT one-loop 2PCF model in redshift space with their Taruya–Nishimichi–Saito (TNS) model (Taruya et al. 2010). For the same reason, we push the analysis down to  $s_{\text{min}} = 5 h^{-1}$  Mpc, but then show the results obtained with larger values up to  $s_{\text{min}} = 15 h^{-1}$  Mpc (our reference case).

The 2D and 1D posterior distributions shown in Fig. 4 agree well with the results of Pezzotta et al. (2017) except for the pairwise velocity dispersion,  $\sigma_{12}$ , which is significantly ( $2\sigma$ ) smaller. This is not surprising since, as shown in fig. 18 of Pezzotta et al. (2017), the Scoccimarro (2004) 2PCF model tends to underestimate the value of  $\sigma_{12}$ .

The 2D contours in Fig. 5 show a mild anticorrelation between  $f\sigma_8$  and  $b_1\sigma_8$ , which is expected since larger redshift distortions that boost up the 2PCF monopole can be compensated by reducing the clustering amplitude  $b_1\sigma_8$ . In addition, we find a positive correlation between  $f\sigma_8$  and  $\sigma_{12}$ , which is explained by the fact that damping effects can be compensated by increasing the clustering amplitude.

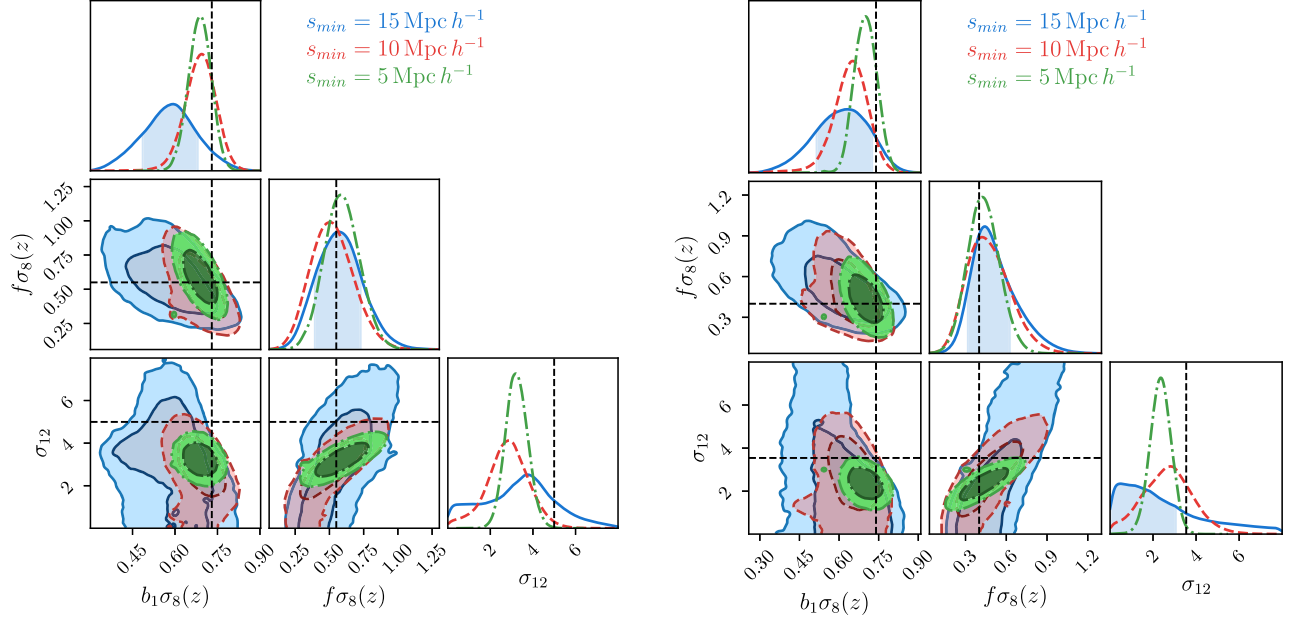


**Figure 5.** Marginalized 2D posterior probability levels for the parameters  $b_1\sigma_8$ ,  $f\sigma_8$ , and  $\sigma_{12}$ , from the 2PCF analysis of the P1 and P2 ‘control’ samples (left/right respectively), as a function of the minimum scale included in the analysis (see legend). The units of  $\sigma_{12}$  are  $h^{-1}$  Mpc and the darker/lighter shades for each set correspond to 68 per cent and 95 per cent confidence levels, respectively. 1D distribution functions on the diagonal give the 1D marginalized probability distributions of each parameter, with the 68 per cent interval indicated by the blue-shaded area for the  $s_{\min} = 15 h^{-1}$  Mpc reference case only. The horizontal and vertical dashed lines give the best-fitting values obtained by Pezzotta et al. (2017) on similar subsamples of the VIPERS PDR2 catalogue.

**Table 3.** Summary of the best-fitting parameter values and their  $1\sigma$  uncertainties, as obtained from the G1/G2 VIPERS samples using the 2PCF-only, 3PCF-only, and joint 2PCF+3PCF analyses. The parameters common to all analyses are  $b_1$ ,  $\gamma$ ,  $\beta$ , and  $\sigma_8$ . For the 2PCF and joint analyses, the pairwise velocity dispersion  $\sigma_{12}$  is also considered. To account for parameter degeneracy, we also list some of the relevant parameter combinations constrained by the individual 2PCF and 3PCF analyses.

Sample	Probe	$\sigma_8(z)$	$b_1$	$\gamma$	$\beta$	$\sigma_{12}$	$f$	$b_1\sigma_8(z)$	$f\sigma_8(z)$
G1	2PCF	–	–	–	$1.2 \pm 0.6$	$2.4 \pm 2.1$	–	$0.56^{+0.12}_{-0.11}$	$0.7 \pm 0.2$
	3PCF	–	–	$0.1^{+0.8}_{-1.3}$	$0.02^{+0.70}_{-0.0}$	–	–	$1.0 \pm 0.3$	$0.0 \pm 0.5$
	Joint	$0.50 \pm 0.12$	$1.60 \pm 0.43$	$-0.1^{+0.8}_{-1.3}$	$0.4^{+0.3}_{-0.2}$	$2.4 \pm 2.0$	$0.64^{+0.55}_{-0.37}$	$0.84^{+0.09}_{-0.14}$	$0.36^{+0.17}_{-0.12}$
G2	2PCF	–	–	–	$0.6^{+0.9}_{-0.3}$	$1.0^{+1.6}_{-1.0}$	–	$0.67^{+0.15}_{-0.17}$	$0.49^{+0.42}_{-0.16}$
	3PCF	–	–	$0.2^{+3.5}_{-1.3}$	$0.0^{+1.4}_{-0.0}$	–	–	$0.4^{+0.5}_{-0.2}$	$0.0^{+0.7}_{-0.0}$
	Joint	$0.39^{+0.11}_{-0.13}$	$1.9^{+0.8}_{-0.5}$	$0.5^{+1.3}_{-1.2}$	$0.49^{+0.31}_{-0.23}$	$1.0^{+1.6}_{-1.0}$	$1.0 \pm 1.0$	$0.74^{+0.07}_{-0.08}$	$0.43^{+0.16}_{-0.15}$

To assess the sensitivity of our results to some of the model parameters, we have performed two robustness tests. In the first one we have repeated the likelihood analysis with different values of  $s_{\min} = 5, 10,$  and  $15 h^{-1}$  Mpc. The results are shown in the same Fig. 5. As expected, increasing the value of  $s_{\min}$  amplifies the errors, especially for the non-linear  $\sigma_{12}$  parameter. However, no systematic error is introduced as all results agree with those of Pezzotta et al. (2017) and with each other.

As a second test we used the alternative 2PCF model introduced in Section 5.3 in which we (1) use HALOFIT (Takahashi et al. 2012) to model  $P_{\delta\delta}$  and (2) adopt the fitting formula of Bel et al. (2019) to model  $P_{\delta\theta}$  and  $P_{\theta\theta}$ . The results are very similar to those obtained with the reference 2PCF model.

Finally, we have repeated the likelihood analysis on G1 and G2 samples that we use for the 3PCF analysis too. The results, which are qualitatively similar to those obtained with P1 and P2, are summarized in Table 3 where we list the best-fitting parameters and their  $1\sigma$  uncertainties.

We confirm that the 2PCF analysis successfully constrains the parameter combinations  $f\sigma_8$ ,  $b_1\sigma_8$ , and  $\beta \equiv f/b_1$  but leave  $\gamma$  unconstrained. This is not surprising since this parameter is sensitive to the small-scale clustering that we ignore, having set  $s_{\min} = 15 h^{-1}$  Mpc. Indeed, when the analysis is extended down to  $s_{\min} = 5 h^{-1}$  Mpc, we do measure a  $\gamma$  value significantly different from zero, yet mildly inconsistent with the results of previous VIPERS analyses (Cappi et al. 2015; Di Porto et al. 2016). This value is also in tension with the one yielded by the 3PCF analysis presented in the next section. It probably indicates the minimum scales below which our galaxy 2PCF model fails and thus justifies our choice of setting  $s_{\min} = 15 h^{-1}$  Mpc.

### 7.2 3PCF

We have repeated the likelihood analysis to compare the 3PCF measurements in the G1 and G2 sample with the 3PCF model described in Section 5.4 and the  $35 \times 35$  covariance matrix  $C_{\zeta, \zeta}$  shown in Fig. 4.

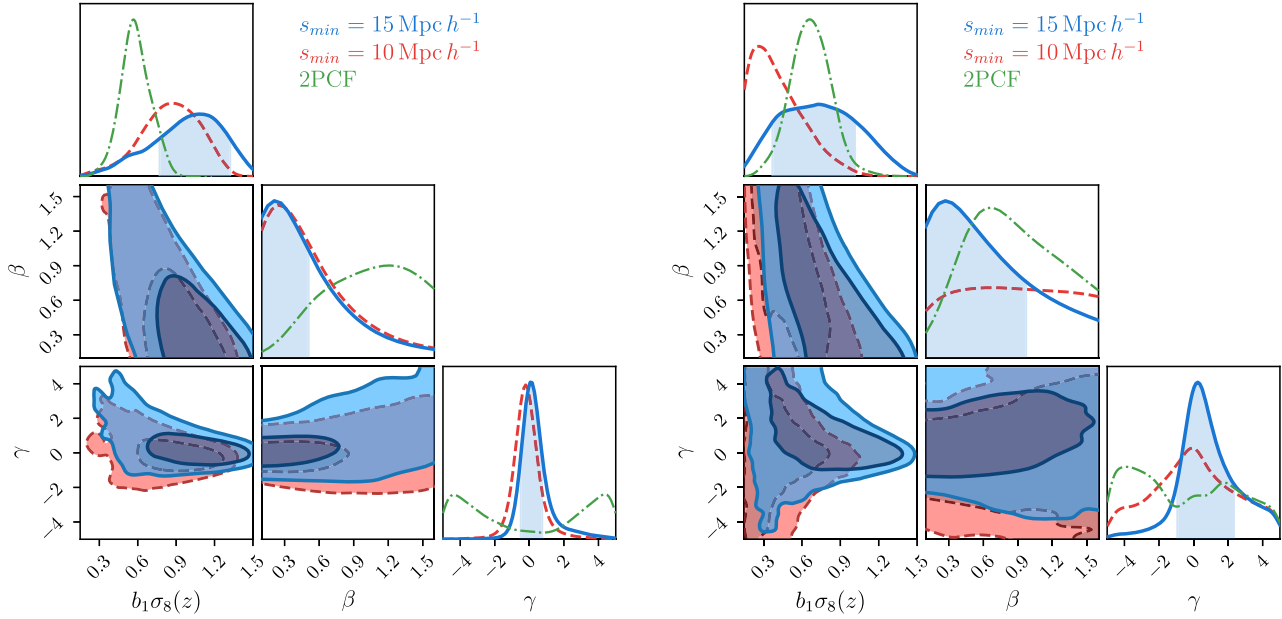


**Figure 6.** Marginalized 2D and 1D posterior distributions for the parameters  $b_1\sigma_8$ ,  $\beta$ , and  $\gamma$ , obtained from the 3PCF analysis of the G1 and G2 VIPERS samples (left- and right-hand panels, respectively). The plots show the results for the two choices of  $s_{\min}$  as indicated by the legend. As in previous figures, darker/lighter shades correspond to 68 per cent and 95 per cent confidence levels, respectively. The green dashed lines report the marginalized 1D distributions obtained for the same parameters from the 2PCF analysis, using  $s_{\min} = 15 h^{-1}$  Mpc.

This analysis improves upon the one performed by Moresco et al. (2017) in different ways. First, we use a more accurate 3PCF model and a covariance matrix estimated from realistic mock catalogues to perform a full likelihood analysis. Secondly, here we use the final, PDR2 release of the VIPERS catalogue. Finally, we consider all triangle configurations and not just a few subsets. We stress the importance of this latter aspect since, in our estimator, we use a triangle representation that is flexible enough to allow us to select subsets of triangles characterized by specific configurations and side lengths, greatly simplifying the comparison with model predictions.

The plots in Fig. 6 are analogous to those of Fig. 5. They show the 2D and 1D marginalized posterior distributions for the parameters  $b_1\sigma_8$ ,  $\beta$ , and  $\gamma$  obtained from the 3PCF measured in the G1 (left) and G2 (right) samples. The best-fitting parameters and their uncertainties are listed in Table 3. The 3PCF analysis allows us to estimate the non-linear bias parameter  $\gamma$ , which turns out to be consistent with zero, while 2PCF is completely insensitive to it, as shown by the green, dot-dashed curves in the bottom right-hand panels. This result is in agreement with Moresco et al. (2017) and marginally consistent with those obtained from counts-in-cells analyses of Cappi et al. (2015) and Di Porto et al. (2016) where a non-zero value of  $\gamma$  was measured but on scales much smaller than those considered here.

The constraints on the distortion parameter  $\beta$  are, on the contrary, quite weak. The best-fitting value of this parameter is consistent with zero within the errors. This is not unexpected since in our analysis we considered only the 3PCF monopole moment, which is insensitive to the RSD effects. Constraints on  $\beta$  could be obtained by considering the 3PCF multipoles. This is, however, beyond the scope of this work since a multipole analysis would require the use of a significantly larger covariance matrix, which cannot be accurately estimated with the 153 mock catalogues at our disposal.

Another interesting feature is the mild degeneracy between  $\beta$  and the clustering amplitude  $b_1\sigma_8$  also seen for the 2PCF. The difference

is that here the error on  $b_1\sigma_8$  from the 3PCF analysis is about three times larger than from the 2PCF one.

To test the sensitivity to the choice of  $s_{\min}$  we repeated the likelihood analysis using  $s_{\min} = 5, 10, 15,$  and  $20 h^{-1}$  Mpc. In Fig. 6, we only show the cases of  $s_{\min} = 10$  and  $15 h^{-1}$  Mpc to avoid overcrowding. When  $s_{\min}$  decreases, the maximum of the 1D posterior distributions for  $b\sigma_8$  shifts to smaller values. However, due to the large errors, the best-fitting values of  $b\sigma_8$  (but also the ones of  $\gamma$  and  $\beta$ ) are in fact consistent with each other for all choices of  $s_{\min}$ . In Appendix C, we present a more detailed study of the impact of  $s_{\min}$  on the parameters' estimates using the VIPERS mock catalogues. Finally, despite their different shapes, the 1D posteriors of all parameters obtained from the 3PCF analysis for all values of  $s_{\min}$  largely overlap those obtained from the 2PCF.

To further assess the impact of non-linear effects, we compared the measured 3PCF with a model including the damping term of equation (26) and varying its strength. The result is shown in Fig. 7, with the reference case with  $\alpha = 0$  corresponding to no damping. We set the pairwise velocity dispersion,  $\sigma_{12}$ , equal to the best-fitting value obtained from the 2PCF analysis. The plot compares model predictions with the 3PCF measured for various triangle shapes, whose side lengths are indicated on the x-axis. The results show that incoherent motions do not significantly affect model predictions on the scales considered in our analysis. They may, however, become relevant for next-generation surveys, in which statistical errors will be significantly smaller than those considered here. We plan to further investigate this aspect and introduce a novel non-linear 3PCF model to tackle the problem.

### 7.3 Joint analysis of 2PCF and 3PCF

Finally, we perform for the first time a joint 2PCF and 3PCF correlation analysis on the VIPERS data. The main goal is to break the parameter degeneracy and obtain individual estimates for  $\sigma_8$ , for the

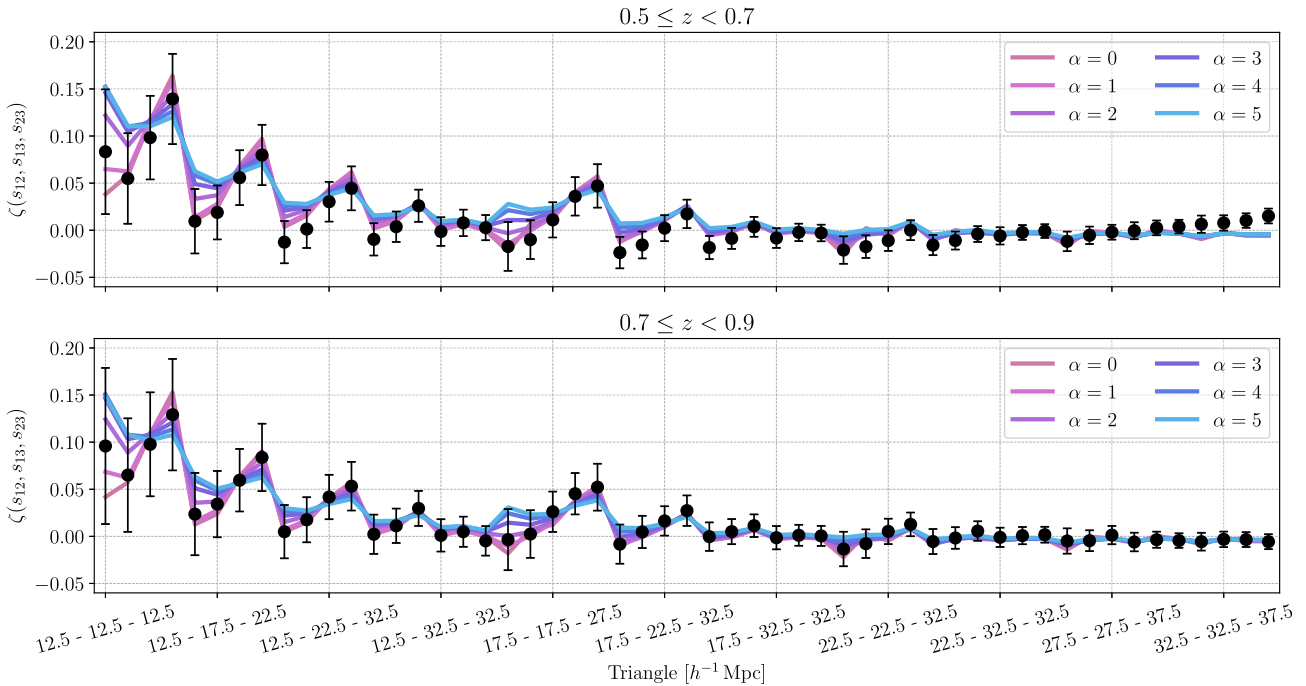


**Figure 7.** The impact of small-scale damping on our model for the 3PCF monopole. The estimated 3PCF from the VIPERS G1 and G2 samples (top and bottom respectively, data and error bars as in Fig. 3) is compared to the theoretical predictions, varying the amplitude of non-linear motions, through the parameter  $\alpha$ . The case  $\alpha = 0$  corresponds to the reference case, in which small-scales non-linear motions are ignored.

linear growth rate  $f$ , and for the two bias parameters  $b_1$  and  $\gamma$ . Fig. 8 shows the 1D and 2D posterior probability distributions (blue regions and solid curves) of these parameters from the likelihood analysis of the G1 and G2 samples and using the full  $45 \times 45$  covariance matrix. The same range of scales  $[15, 40] \text{ Mpc } h^{-1}$  was considered in both the two- and three-point statistics. The 1D posterior distributions obtained from the 2PCF-only (green, dot-dashed) and 3PCF-only (red, dashed) analyses are also shown for reference. The best-fitting values of the joint analysis and their uncertainties are listed in Table 3.

The joint analysis successfully breaks the  $\sigma_8$ - $b_1$ - $f$  degeneracy, and the parameters can be measured individually, although with different uncertainties. The value of  $\sigma_8$  is measured with a  $\sim 20$  per cent uncertainty in both G1 and G2 samples. The error on  $b_1$  is  $\sim 20$  per cent in the G1 sample, increasing to  $\sim 30$  per cent in G2. The error on the growth rate  $f$  is significantly larger (65–75 per cent), reflecting the fact that the  $f$ - $\sigma_8$  degeneracy is only partially broken by our analysis. Though significantly less precise, it is reassuring that our best-fitting  $\sigma_8$  and  $f$  values are in agreement with those of the Planck Collaboration VI (2020) cosmology, scaled to the redshift of the survey (vertical and horizontal dashed lines). The sensitivity of these results to the choice of  $s_{\min}$  is thoroughly discussed in Appendix C.

The joint analysis does not improve the estimate of  $\gamma$ , whose precision is driven by the 3PCF signal, as shown in Fig. 8. It does instead improve the estimate of  $\sigma_{12}$  whose value, in agreement with the one obtained from the 2PCF analysis, is estimated with a significantly higher precision.

Overall, the results of the joint analysis clearly show that the degeneracy of some parameters are successfully broken, thanks to the ability to extract information from intermediate to small scales where non-linear effects are relevant, both in the evolution of the density fluctuation and in the biasing relation.

## 8 DISCUSSION AND CONCLUSIONS

In this work, we have measured the 2PCF and 3PCF of the galaxies in the final data release of the VIPERS survey and used their joint information to break parameter degeneracies and estimate the galaxy bias parameters,  $b_1$  and  $\gamma$ , the clustering amplitude,  $\sigma_8$ , and the linear growth rate of density fluctuations,  $f$ , at two redshifts  $z \simeq 0.61$  and  $z \simeq 0.8$ .

Because of the survey footprint, separated in two patches highly elongated in one direction, we performed the analysis in configuration space focusing on scales smaller than  $40 h^{-1} \text{ Mpc}$ . To do so, we adopted a one-loop anisotropic 2PCF model to account for non-linear effects, galaxy bias, and redshift distortions. For the 3PCF we considered the tree-level model of its monopole moment in redshift space proposed by Slepian et al. (2017b). To estimate the 3PCF we have used the SHD method of Slepian & Eisenstein (2015) whose efficiency allowed us to measure the 3PCF of all 153 mock VIPERS catalogues and thus to estimate the covariance matrix used in the likelihood analysis. Because of all these aspects, we believe that our analysis improves over the previous joint 2PCF and 3PCF analysis of the WiggleZ galaxy sample that was performed by Marín et al. (2013) using the brute-force triplet counting estimator simplified analytic models for 2PCF, 3PCF, and their covariance matrix.

The main results of this work can be summarized as follow.

(i) When we use the P1 and P2 data sets, the results of our 2PCF analysis agree, as expected, with those obtained by Pezzotta et al. (2017) in the range  $[5, 50] h^{-1} \text{ Mpc}$ , despite having used a different covariance matrix and a different 2PCF model. Indeed, our estimates of

$$f\sigma_8(z = 0.61) = 0.58 \pm 0.12,$$

$$f\sigma_8(z = 0.87) = 0.43 \pm 0.12$$

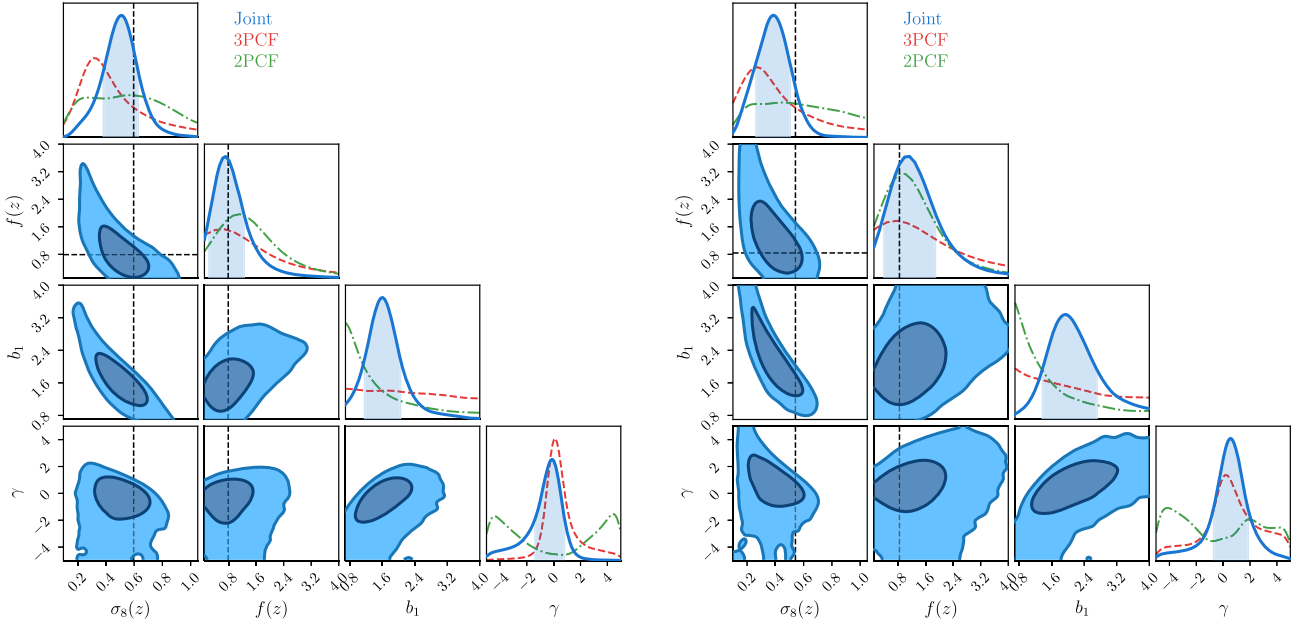


**Figure 8.** Marginalized 1D and 2D posterior distributions for the parameters  $\sigma_8(z)$ ,  $f(z)$ , and  $b_1$ , from the joint 2PCF+3PCF analysis of the G1 and G2 VIPERS samples (left- and right-hand panels, respectively). All estimates use  $s_{\min} = 15 h^{-1}$  Mpc. The meaning of contours and shaded areas is as in Fig. 6. The vertical and horizontal black dashed lines show for reference the values measured for the same parameters by Planck Collaboration VI (2020), self-consistently scaled to the corresponding VIPERS redshift.

and

$$b_1\sigma_8(z = 0.61) = 0.69 \pm 0.04,$$

$$b_1\sigma_8(z = 0.87) = 0.70 \pm 0.04$$

match those of Pezzotta et al. (2017) ( $f\sigma_8(z = 0.61) = 0.55 \pm 0.12$ ,  $f\sigma_8(z = 0.87) = 0.40 \pm 0.11$ ;  $b_1\sigma_8(z = 0.61) = 0.73 \pm 0.03$ ,  $b_1\sigma_8(z = 0.87) = 0.74 \pm 0.04$ ).

When we consider pairs with  $s_{\min} \geq 10 h^{-1}$  Mpc the 1D posterior probability distribution of  $\gamma \equiv b_2/b_1$  is flat, whereas it peaks at negative values when pairs at separations as small as  $5 h^{-1}$  Mpc are included. Since a negative value is neither confirmed by previous VIPERS analyses (Cappi et al. 2015; Di Porto et al. 2016) nor by our joint 2PCF and 3PCF analysis, we consider it as a piece of evidence that the 2PCF model is inadequate to describe galaxy clustering on such small scales. Moreover, we found that including pairs with separations larger than  $40 h^{-1}$  Mpc, where shot noise starts to be significant, increases the computational cost of a less accurate covariance matrix, and does not improve the quality of the fit.

For all these reasons, we focused on a smaller scale range  $[15, 40] h^{-1}$  Mpc, and then assessed the robustness of our results to this choice. We then repeated the 2PCF analysis of G1 and G2 samples using this range and found  $f\sigma_8(z = 0.61) = 0.47_{-0.15}^{+0.17}$ . This is in good agreement with the estimates of de la Torre et al. (2017),  $f\sigma_8(z = 0.6) = 0.48 \pm 0.11$ , and of Gil-Marín et al. (2017),  $f\sigma_8(z = 0.57) = 0.432 \pm 0.022$ . Our measurements are shown in Fig. 9 together with existing estimates of  $f\sigma_8$  obtained at different redshifts. As evident, there is an excellent agreement with previous results and with the theoretical expectation of a Planck cosmology (Planck Collaboration VI 2020).

(ii) We measured the 3PCF of the G1 and G2 samples in the same range as the 2PCF,  $[15, 40] h^{-1}$  Mpc, for all triangle configurations. We compared these measurements with the model predictions to

estimate the bias parameters  $b_1$  and  $\gamma$  (for the remaining parameters we have the assumed a local Lagrangian bias model). We found  $\gamma(z = 0.61) = 0.1_{-1.3}^{+0.8}$  and  $\gamma(z = 0.8) = 0.2_{-1.3}^{+3.5}$ , in tension with the result of Moresco et al. (2017) ( $\gamma(z \simeq 0.6) = -0.47 \pm 0.144$ ). The mismatch probably reflects the different scales probed by the two cases, since Moresco et al. (2017) pushed their analysis to scales as small as  $1 h^{-1}$  Mpc (and fixed all parameters of the model except  $b_1$  and  $b_2$ ).

Di Porto et al. (2016) estimated the biasing function from a count-in-cells analysis of the first data release of VIPERS. Among the shape parameters are used to characterize the biasing function in that analysis the one dubbed  $B \equiv [1 - \tilde{b}/\hat{b}]$  can be directly compared to  $\gamma$ . The measured  $B$  values at the redshifts of the G1 and G2 samples and on the scale of  $8 h^{-1}$  Mpc ( $B(z = 0.6) = 0.007 \pm 0.006$  and  $B(z = 0.8) = 0.005 \pm 0.005$ ) agree with our estimates of  $\gamma$ .

Cappi et al. (2015) also performed counts in cells to derive volume-averaged higher order correlation functions from which they inferred the bias parameters  $b_1$  and  $b_2$ . The scales considered in their analyses and the magnitude cuts are, however, different from ours. Nevertheless, it is reassuring that, similarly to our case, they did not detect significant deviations from a linear biasing.

(iii) We have shown that a joint two- and three-point correlation analysis of the VIPERS samples successfully breaks the degeneracy among  $\sigma_8$ ,  $f$ , and  $b_1$  (and, consequently,  $b_2$ ) and reduces the errors in the estimate of their combinations  $f\sigma_8$ ,  $b_1\sigma_8$ , and  $f/b_1$ . It is instructive to compare our results to those of similar analyses, aimed at breaking parameter degeneracies by combining two- and three-point statistics in configuration (Marín et al. 2013) and Fourier space (Gil-Marín et al. 2017) and by combining clustering and gravitational lensing measurements using the VIPERS PDR2 data (de la Torre et al. 2017).

Our estimates of the clustering amplitude,  $\sigma_8(z = 0.61) = 0.50 \pm 0.12$  and  $\sigma_8(z = 0.8) = 0.39_{-0.13}^{+0.11}$ , are in good agreement with those obtained by de la Torre et al. (2017) ( $\sigma_8(z = 0.6) =$

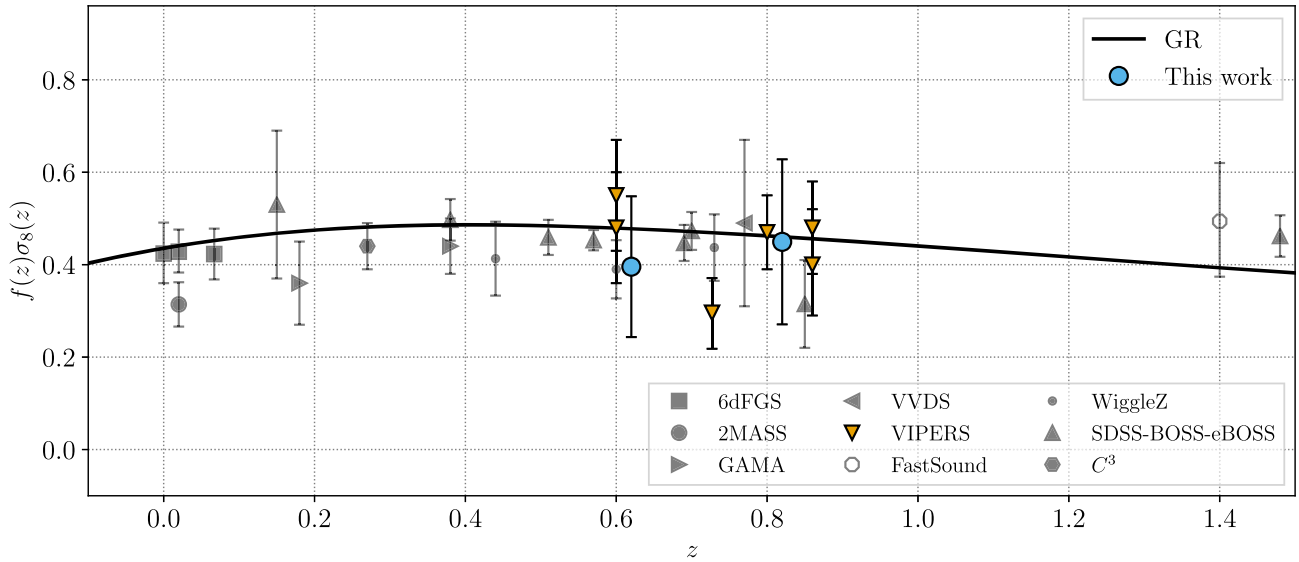


**Figure 9.** Comparison of our new estimates of the growth rate of structure, parametrized by the product  $f\sigma_8$  (light blue circles), with previous measurements from the literature: 6dFGS (Beutler et al. 2012; Adams & Blake 2017; Huterer et al. 2017); Two Micron All-Sky Survey (2MASS; Davis et al. 2011); Galaxy And Mass Assembly (GAMA; Blake et al. 2013); WiggleZ (Blake et al. 2012); VIMOS-VLT Deep Survey (VVDS; Guzzo et al. 2008); VIPERS (de la Torre et al. 2013, 2017; Hawken et al. 2017; Pezzotta et al. 2017; Mohammad et al. 2018); FastSound (Okumura et al. 2016); SDSS+BOSS+eBOSS (Alam et al. 2021), ‘ $C^3$  – Cluster Clustering Cosmology’ (Marulli et al. 2020). The black solid line shows the  $\Lambda$ CDM+GR Planck Collaboration VI (2020) model prediction.

$0.52 \pm 0.06$  and  $\sigma_8(z = 0.86) = 0.48 \pm 0.04$ , Marín et al. (2013) ( $\sigma_8(z = 0.55) = 0.61^{+0.08}_{-0.09}$ ), Gil-Marín et al. (2017) ( $\sigma_8(z = 0.57) = 0.66 \pm 0.067$ ), and with the *Planck*  $\Lambda$ CDM predictions, as shown in the right-hand panel of Fig. 10.

Similarly, our estimates of the growth rate  $f(z = 0.61) = 0.64^{+0.55}_{-0.37}$  and  $f(z = 0.8) = 1.0 \pm 1.0$  agree with those of de la Torre et al. (2017) ( $f(z = 0.6) = 0.93 \pm 0.22$  and  $f(z = 0.86) = 0.99 \pm 0.19$ ) and Gil-Marín et al. (2017) ( $f(z = 0.57) = 0.649 \pm 0.076$ ) within the error that is much larger in our case. All these measurements are shown in the left-hand panel of Fig. 10 together with the *Planck*  $\Lambda$ CDM predictions (Planck Collaboration VI 2020).

We notice that the errors on both  $f$  and  $\sigma_8$  in our case are significantly larger than in de la Torre et al. (2017), despite having used similar data sets. The reason for this is twofold. First of all, we have adopted a more conservative approach and considered  $s_{\min} = 15 h^{-1}$  Mpc, whereas de la Torre et al. (2017) used  $s_{\min} = 5 h^{-1}$  Mpc. This choice, motivated by the discrepant  $\gamma$  value found in the 2PCF analysis, prevents us from accessing information encoded on smaller scales. If these are included, then the errors in the measured  $f$  and  $\sigma_8$  significantly decrease towards values comparable to those of de la Torre et al. (2017), as illustrated in Appendix C. The second reason is that the clustering–lensing analysis is more efficient in breaking parameter degeneracy than the joint 2PCF–3PCF. In fact, the latter combines the galaxy 2PCF, which has a  $b_1\sigma_8$  degeneracy, to the galaxy 3PCF, which has a similar degeneracy,  $b_1^2\sigma_8^2$ . On the contrary, the lensing analysis has a  $b_1\sigma_8^2$  degeneracy, which is effectively broken when combined with the galaxy 2PCF.

(iv) We have performed many tests to check the robustness of our results against non-linear effects, which are expected to be relevant on the scales probed here and are the reason for the conservative cut at  $s_{\min} = 15 h^{-1}$  Mpc. Decreasing  $s_{\min}$  reduces parameters errors from the 2PCF-only analysis but also picks up a negative value for  $\gamma$ , in mild tension (given the considerable uncertainty) with the joint 2PCF–3PCF analysis and previous VIPERS analyses. On the

contrary, reducing  $s_{\min}$  does not have a significant impact on the 3PCF and the joint analyses. In Table 4, we list the best-fitting values of  $\sigma_8, f, b_1$ , and  $\gamma$  obtained for different choices of  $s_{\min}$ . Errors increase when  $s_{\min}$  increases, as a result of the reduction of the number of pairs/triplets and scales included in the analysis. In particular, with  $s_{\min} = 20 h^{-1}$  Mpc no significant constraints can be set on  $\gamma$ . A detailed analysis of the sensitivity of our results to the choice of  $s_{\min}$  is presented in Appendix C.

Our work confirms the importance of clustering analyses beyond two-point statistics. Here, we were able to break parameter degeneracies using a relatively modest number of objects (23 352 and 13 046 for the G1 and G2 samples, respectively). In this respect, this work represents a successful pilot study in the preparation for the next generation spectroscopic surveys, such as the DESI project, the *Euclid* (Laureijs et al. 2011), and the *Roman* (Akeson et al. 2019) space telescope missions. These surveys will be able to perform clustering analyses on scales much larger than those considered here. However, small scales will still encode an even larger amount of information. Its extraction will require measuring higher order statistics and comparing results to non-linear models, as we have done in this work. In this respect, one of the main lessons learned from our analysis is the need to develop a full one-loop model for the 3PCF, matching the 2PCF one, which we plan to present in future work.

The availability of such a model, along with that of a new generation of efficient 3PCF estimators (Slepian & Eisenstein 2015, 2016), would make higher order clustering analyses in configuration space more palatable and a serious contender to more traditional Fourier-space methods. Bispectrum analyses enjoy the availability of fast estimators and non-linear models. However, they suffer from mode coupling induced by complex survey geometries, which is difficult to account for. Comparing the performances of joint two- and three-point clustering analyses in configuration and Fourier space for

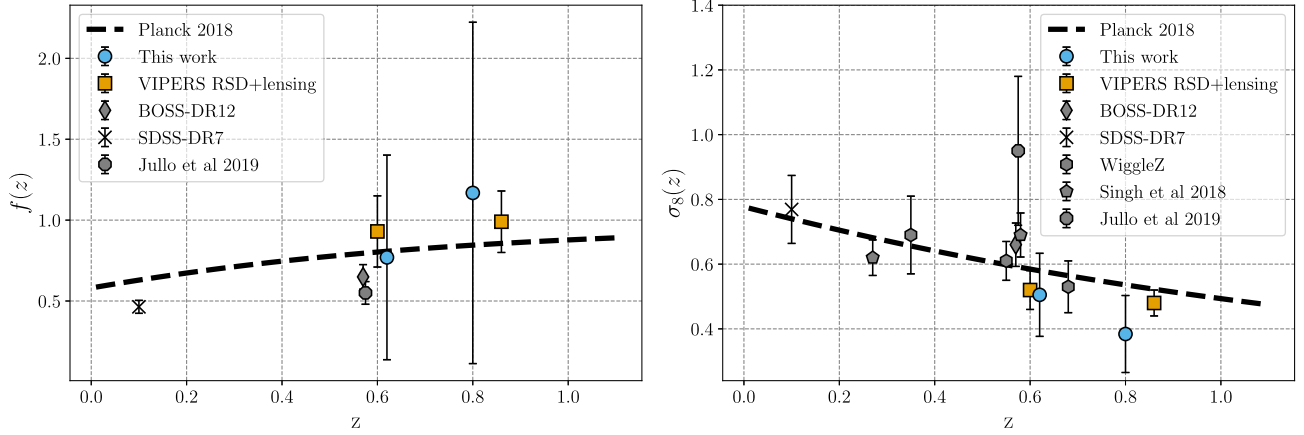


**Figure 10.** Values for  $f(z)$  (left-hand panel) and  $\sigma_8(z)$  (right-hand panel), as estimated from our joint 2PCF and 3PCF analysis (light blue circles), again compared to other recent measurements using different techniques: VIPERS joint lensing–RSD analysis (de la Torre et al. 2017), BOSS DR12  $P(k) + B(k)$  analysis (Gil-Marín et al. 2017), and Wiggle-z  $\xi + \zeta$  analysis (Marín et al. 2013). For completeness, we also include results at smaller redshifts by Shi et al. (2018) (joint lensing–RSD analysis), Singh et al. (2019) (joint analysis of galaxy and CMB lensing and SDSS spectroscopy), and Jullo et al. (2019) (BOSS DR12 RSD+lensing analysis).

**Table 4.** Best-fitting values of the parameters obtained in the joint analysis of 2PCF and 3PCF, using different values of  $s_{\min}$ . The values of  $s_{\min}$  are in  $h^{-1}$  Mpc. All the constraints are compatible within  $1\sigma$ .

Sample	$s_{\min}$	$\sigma_8(z)$	$f$	$b_1$	$\gamma$
G1	10	$0.4 \pm 0.1$	$1.0^{+0.7}_{-0.5}$	$1.8^{+0.4}_{-0.3}$	$-0.1 \pm 0.6$
	15	$0.5 \pm 0.1$	$0.6^{+0.6}_{-0.4}$	$1.6 \pm 0.4$	$-0.1^{+0.9}_{-1.3}$
	20	$0.4^{+0.3}_{-0.2}$	$1.1^{+1.6}_{-1.0}$	$0.5^{+0.7}_{-0.4}$	Unconstrained
G2	10	$0.3 \pm 0.1$	$1.4^{+1.2}_{-0.8}$	$2.0^{+1.0}_{-0.6}$	$-1.1^{+1.4}_{-2.2}$
	15	$0.4 \pm 0.1$	$1.0 \pm 1.0$	$1.9^{+0.8}_{-0.5}$	$0.5^{+1.3}_{-1.2}$
	20	$0.2^{+0.2}_{-0.1}$	$0.9^{+1.4}_{-0.8}$	$1.8^{+1.9}_{-0.9}$	$-0.2^{+1.5}_{-3.9}$

next-generation spectroscopic surveys is another open issue, which we plan to investigate in the future.

Finally, in this analysis, we were able to break parameter degeneracies using higher order statistics. Alternatively, it can be broken by combining two-point clustering and gravitational lensing, as in de la Torre et al. (2017). Both approaches have advantages and disadvantages. The two- and three-point clustering analysis requires a single (spectroscopic) data set to be performed. However, it is less efficient in removing parameters’ degeneracy. The clustering–lensing analysis is more effective in breaking degeneracy but needs both a photometric and a spectroscopic survey to be performed. How to best combine these two types of analyses is another interesting issue that deserves a dedicated future study.

## ACKNOWLEDGEMENTS

AV and EB thank Emiliano Sefusatti, Alexander Eggemeier, Elena Sarpa, and Massimo Guidi for useful discussions. This paper uses data from the VIMOS Public Extragalactic Redshift Survey (VIPERS). VIPERS has been performed using the ESO Very Large Telescope, under the ‘Large Programme’ 182.A-0886. The participating institutions and funding agencies are listed at <http://vipers.inaf.it>. AV, EB, LG, and LM are supported by ASI/INAF agreement no. 2018-23-HH.0 ‘Scientific Activity for *Euclid* Mission, Phase D’ and INFN Project ‘InDark’. EB and LG are further

supported by MIUR/PRIN 2017 ‘From Darklight to Dark Matter: Understanding the Galaxy–Matter Connection to Measure the Universe’. EB is also supported by ASI/INAF agreement no. 2017-14-H.O ‘Unveiling Dark Matter and Missing Baryons in the High-Energy Sky’. MM acknowledges the grants ASI no. I/023/12/0, ASI no. 2018-23-HH.0, and support from MIUR, PRIN 2017 (grant 20179ZF5KS). This research was supported by the Munich Institute for Astro- and Particle Physics (MIAPP) that is funded by the Deutsche Forschungsgemeinschaft (DFG, German Research Foundation) under Germany’s Excellence Strategy – EXC – 2094 - 390783311. LM also acknowledges the support from the grant PRIN-MIUR 2017 WSCC32.

## DATA AVAILABILITY

The VIPERS PDR2 data, as well as the mock samples, used here are publicly available from the VIPERS web site (<http://vipers.inaf.it>). The clustering measurements and covariance matrices from this paper are available from the authors, upon request.

## REFERENCES

- Adams C., Blake C., 2017, *MNRAS*, 471, 839  
Akeson R. et al., 2019, preprint ([arXiv:1902.05569](https://arxiv.org/abs/1902.05569))  
Alam S. et al., 2017, *Phys. Rev. D*, 103, 083533  
Alcock C., Paczynski B., 1979, *Nature*, 281, 358  
Bel J., Pezzotta A., Carbone C., Sefusatti E., Guzzo L., 2019, *A&A*, 622, A109  
Beutler F. et al., 2012, *MNRAS*, 423, 3430  
Blake C. et al., 2012, *MNRAS*, 425, 405  
Blake C. et al., 2013, *MNRAS*, 436, 3089  
Cappi A. et al., 2015, *A&A*, 579, A70  
Cole S. et al., 2005, *MNRAS*, 362, 505  
Davidzon I. et al., 2016, *A&A*, 586, A23  
Davis M., Nusser A., Masters K. L., Springob C., Huchra J. P., Lemson G., 2011, *MNRAS*, 413, 2906  
de la Torre S. et al., 2013, *A&A*, 557, A54  
de la Torre S. et al., 2017, *A&A*, 608, A44  
DESI Collaboration, 2016a, preprint ([arXiv:1611.00036](https://arxiv.org/abs/1611.00036))  
DESI Collaboration, 2016b, preprint ([arXiv:1611.00037](https://arxiv.org/abs/1611.00037))  
Di Porto C. et al., 2016, *A&A*, 594, A62

- Eisenstein D. J. et al., 2005, *ApJ*, 633, 560
- Fry J. N., 1994, *Phys. Rev. Lett.*, 73, 215
- Garilli B. et al., 2014, *A&A*, 562, A23
- Gil-Marín H., Noreña J., Verde L., Percival W. J., Wagner C., Manera M., Schneider D. P., 2015, *MNRAS*, 451, 539
- Gil-Marín H., Percival W. J., Verde L., Brownstein J. R., Chuang C.-H., Kitaura F.-S., Rodríguez-Torres S. A., Olmstead M. D., 2017, *MNRAS*, 465, 1757
- Granett B. R., Favole G., Montero-Dorta A. D., Branchini E., Guzzo L., de la Torre S., 2019, *MNRAS*, 489, 653
- Guo H., Li C., Jing Y. P., Börner G., 2014, *ApJ*, 780, 139
- Guo H. et al., 2015, *MNRAS*, 449, L95
- Guzzo L. et al., 2008, *Nature*, 451, 541
- Guzzo L. et al., 2014, *A&A*, 566, A108
- Hartlap J., Simon P., Schneider P., 2007, *A&A*, 464, 399
- Hawken A. J. et al., 2017, *A&A*, 607, A54
- Howlett C., Lewis A., Hall A., Challinor A., 2012, *J. Cosmol. Astropart. Phys.*, 04, 027
- Hui L., Gaztañaga E., 1999, *ApJ*, 519, 622
- Huterer D., Linder E. V., 2007, *Phys. Rev. D*, 75, 023519
- Huterer D., Shafer D. L., Scolnic D. M., Schmidt F., 2017, *J. Cosmol. Astropart. Phys.*, 05, 015
- Jing Y. P., Börner G., 2004, *ApJ*, 607, 140
- Jullo E. et al., 2019, *A&A*, 627, A137
- Kayo I. et al., 2004, *PASJ*, 56, 415
- Kazin E. A. et al., 2013, *MNRAS*, 435, 64
- Klypin A., Yepes G., Gottlöber S., Prada F., Heß S., 2016, *MNRAS*, 457, 4340
- Kulkarni G. V., Nichol R. C., Sheth R. K., Seo H.-J., Eisenstein D. J., Gray A., 2007, *MNRAS*, 378, 1196
- Landy S. D., Szalay A. S., 1993, *ApJ*, 412, 64
- Laureijs R. et al., 2011, preprint (arXiv:1110.3193)
- Lewis A., Challinor A., Lasenby A., 2000, *ApJ*, 538, 473
- Maartens R., Abdalla F. B., Jarvis M., Santos M. G., 2015, preprint (arXiv:1501.04076)
- McBride C. K., Connolly A. J., Gardner J. P., Scranton R., Newman J. A., Scoccimarro R., Zehavi I., Schneider D. P., 2011a, *ApJ*, 726, 13
- McBride C. K., Connolly A. J., Gardner J. P., Scranton R., Scoccimarro R., Berlind A. A., Marín F., Schneider D. P., 2011b, *ApJ*, 739, 85
- McDonald P., Roy A., 2009, *J. Cosmol. Astropart. Phys.*, 08, 020
- Marín F., 2011, *ApJ*, 737, 97
- Marín F. A. et al., 2013, *MNRAS*, 432, 2654
- Marulli F., Bianchi D., Branchini E., Guzzo L., Moscardini L., Angulo R. E., 2012, *MNRAS*, 426, 2566
- Marulli F. et al., 2013, *A&A*, 557, A17
- Marulli F., Veropalumbo A., Moresco M., 2016, *Astron. Comput.*, 14, 35
- Marulli F., Veropalumbo A., García-Farieta J. E., Moresco M., Moscardini L., Cimatti A., 2020, preprint (arXiv:2010.11206)
- Matarrese S., Verde L., Heavens A. F., 1997, *MNRAS*, 290, 651
- Mohammad F. G. et al., 2018, *A&A*, 610, A59
- Moresco M. et al., 2017, *A&A*, 604, A133
- Moresco M., Veropalumbo A., Marulli F., Moscardini L., Cimatti A., 2020, preprint (arXiv:2011.04665)
- Nichol R. C. et al., 2006, *MNRAS*, 368, 1507
- Okumura T. et al., 2016, *PASJ*, 68, 38
- Peacock J. A. et al., 2001, *Nature*, 410, 169
- Percival W. J. et al., 2014, *MNRAS*, 439, 2531
- Pezzotta A. et al., 2017, *A&A*, 604, A33
- Planck Collaboration VI, 2020, *A&A*, 641, A6
- Rota S. et al., 2017, *A&A*, 601, A144
- Saito S., Baldauf T., Vlah Z., Seljak U., Okumura T., McDonald P., 2014, *Phys. Rev. D*, 90, 123522
- Scoccimarro R., 2004, *Phys. Rev. D*, 70, 083007
- Scoccimarro R., Zaldarriaga M., Hui L., 1999, *ApJ*, 527, 1
- Scodreggio M. et al., 2018, *A&A*, 609, A84
- Sefusatti E., Crocce M., Pueblas S., Scoccimarro R., 2006, *Phys. Rev. D*, 74, 023522
- Sellentin E., Heavens A. F., 2016, *MNRAS*, 456, L132
- Sereno M., Veropalumbo A., Marulli F., Covone G., Moscardini L., Cimatti A., 2015, *MNRAS*, 449, 4147
- Shi F. et al., 2018, *ApJ*, 861, 137
- Singh S., Alam S., Mandelbaum R., Seljak U., Rodríguez-Torres S., Ho S., 2019, *MNRAS*, 482, 785
- Slepian Z., Eisenstein D. J., 2015, *MNRAS*, 454, 4142
- Slepian Z., Eisenstein D. J., 2016, *MNRAS*, 455, L31
- Slepian Z., Eisenstein D. J., 2017, *MNRAS*, 469, 2059
- Slepian Z. et al., 2017a, *MNRAS*, 468, 1070
- Slepian Z. et al., 2017b, *MNRAS*, 469, 1738
- Szapudi I., 2004, *ApJ*, 605, L89
- Szapudi I., Szalay A. S., 1998, *ApJ*, 494, L41
- Takahashi R., Sato M., Nishimichi T., Taruya A., Oguri M., 2012, *ApJ*, 761, 152
- Taruya A., Nishimichi T., Saito S., 2010, *Phys. Rev. D*, 82, 063522
- Wang L., Steinhardt P. J., 1998, *ApJ*, 508, 483
- Yankelevich V., Porciani C., 2019, *MNRAS*, 483, 2078

## APPENDIX A: 3PCF ESTIMATOR BINNING

The algorithm of Slepian & Eisenstein (2015) used in this work estimates the multipole coefficients of the 3PCF Legendre expansion in radial bins  $\Delta_{r_{12}}$  and  $\Delta_{r_{13}}$ ,  $\zeta_l(\Delta_{r_{12}}, \Delta_{r_{13}})$ . To obtain an unbiased estimate of  $\zeta(\Delta_{r_{12}}, \Delta_{r_{13}}, \Delta_\mu)$  in bins  $\Delta_\mu$ , one needs to use bin-averaged Legendre polynomials  $\overline{\mathcal{P}}_l(\Delta_\mu)$ , i.e.

$$\zeta(\Delta_{r_{12}}, \Delta_{r_{13}}, \Delta_\mu) = \sum_{l=0}^{l_{\max}} \zeta_l(\Delta_{r_{12}}, \Delta_{r_{13}}) \overline{\mathcal{P}}_l(\Delta_\mu), \quad (\text{A1})$$

where

$$\begin{aligned} \overline{\mathcal{P}}_l(\Delta_\mu) &\equiv \overline{\mathcal{P}}_l(\mu_{\min} \leq \mu \leq \mu_{\max}) \\ &= \frac{1}{\Delta_\mu} \left[ \frac{\mathcal{P}_{l+1}(\mu) - \mathcal{P}_{l-1}(\mu)}{2l+1} \right]_{\mu_{\min}}^{\mu_{\max}}, \end{aligned} \quad (\text{A2})$$

in the bin  $\Delta_\mu = [\mu_{\min}, \mu_{\max}]$ ; when  $l=0$ ,  $\overline{\mathcal{P}}_{l=0}(\Delta_\mu) = 1$ .

In this work, we express the 3PCF as a function of  $r_{23}$ , rather than  $\mu$ , with the two quantities related through the relation

$$\mu = \frac{r_{12}^2 + r_{13}^2 - r_{23}^2}{2r_{12}r_{13}}, \quad (\text{A3})$$

so that, given  $r_{12}$  and  $r_{13}$ , the cosine angle  $\mu$  varies in the range  $[0, 1]$ , whereas  $r_{23}$  varies between  $|r_{12} - r_{13}|$  and  $|r_{12} + r_{13}|$ . One can show that in this case the binned Legendre polynomials are of the form

$$\begin{aligned} \overline{\mathcal{P}}_l(\Delta_{r_{12}}, \Delta_{r_{13}}, \Delta_{r_{23}}) &= \frac{32\pi}{V_{12}V_{13}} \int k^2 I_l(k; \Delta_{r_{12}}) I_l(k; \Delta_{r_{13}}) \\ &\quad \times I_0(k; \Delta_{r_{23}}) dk, \end{aligned} \quad (\text{A4})$$

where  $V_{12}$  and  $V_{13}$  represent the volume of the spherical shells of width  $\Delta_{r_{12}}$  and  $\Delta_{r_{13}}$ , respectively, and

$$I_l(k; \Delta_r) = \int_{r_{\min}}^{r_{\max}} r^2 j_l(kr) dr, \quad (\text{A5})$$

where  $j_l(kr)$  are spherical Bessel functions.



## APPENDIX B: EXPLICIT EXPRESSIONS FOR THE 3PCF MODEL

The explicit expression of the  $A_l$  terms that appear in equation (25) is

$$\begin{aligned}
 A_0 &= b_1^3 \left\{ \frac{34}{21} \left[ 1 + \frac{4}{3}\beta + \frac{1154}{1275}\beta^2 + \frac{936}{2975}\beta^3 + \frac{21}{425}\beta^4 \right] \right. \\
 &\quad \left. + \gamma \left[ 1 + \frac{2}{3}\beta + \frac{1}{9}\beta^2 \right] + \frac{16}{675}\beta^2\gamma' \right\}, \\
 A_1 &= -b_1^3 \left[ 1 + \frac{4}{3}\beta + \frac{82}{75}\beta^2 + \frac{12}{25}\beta^3 + \frac{3}{35}\beta^4 \right], \\
 A_2 &= b_1^3 \left\{ \frac{8}{21} \left[ 1 + \frac{4}{3}\beta + \frac{52}{21}\beta^2 + \frac{81}{49}\beta^3 + \frac{12}{35}\beta^4 \right] \right. \\
 &\quad \left. + \frac{32\gamma}{945}\beta^2 + \frac{5}{2} \left( \frac{8}{15} + \frac{16\beta}{45} + \frac{344\beta^2}{4725} \right) \gamma' \right\}, \\
 A_3 &= -b_1^3 \left[ \frac{8}{75}\beta^2 + \frac{16}{175}\beta^3 + \frac{8}{315}\beta^4 \right], \\
 A_4 &= b_1^3 \left[ -\frac{32}{3675}\beta^2 + \frac{32}{8575}\beta^3 + \frac{128}{11025} \right]. \tag{B1}
 \end{aligned}$$

In the same equation, the  $f_l$  terms are

$$\begin{aligned}
 f_l(r_{12}, r_{13}, r_{23}) &= \begin{cases} \xi^{[l]}(r_{12})\xi^{[l]}(r_{13})\mathcal{L}_l(\mu_{23}) + \text{cyc.} & \text{if } l \text{ is even,} \\ \left[ \xi^{[l+1]}(r_{12})\xi^{[l-1]}(r_{13}) \right. \\ \quad \left. + \xi^{[l+1]}(r_{13})\xi^{[l-1]}(r_{12}) \right] \mathcal{L}_l(\mu_{23}) + \text{cyc.} & \text{if } l \text{ is odd,} \end{cases} \tag{B2}
 \end{aligned}$$

where

$$\begin{aligned}
 \xi_i^{[l]} &= \int \frac{k^2 dk}{2\pi^2} 2\pi^2 P_{\text{lin}}(k) j_l(kr_i), \\
 \xi_i^{[l\pm]} &= \int \frac{k^2 dk}{2\pi^2} k^{\pm 1} P_{\text{lin}}(k) j_l(kr_i), \tag{B3}
 \end{aligned}$$

and  $P_{\text{lin}}(k)$  is the linear matter power spectrum.

## APPENDIX C: SENSITIVITY TO NON-LINEAR EFFECTS

Since our clustering analysis includes scales smaller than  $40 h^{-1}$  Mpc, non-linear effects in both dynamics and galaxy bias cannot be neglected. To minimize the impact of potential systematic errors derived from an incorrect model of these effects, we have adopted a conservative approach and excluded scales below  $15 h^{-1}$  Mpc from the analysis. These are scales, however, where a significant amount of cosmological information is stored. In this appendix, we use the realistic mock VIPERS catalogues to perform several tests to assess the sensitivity of our results to the choice of this minimum scale,  $s_{\text{min}}$ . We are confident that these tests provide useful indications for the real data analysis since, as we have discussed in Section 3, the 2PCF and 3PCF measured in the mocks agree well with those measured on the real data on all scales considered here.

Let us first consider the parameter combination  $f\sigma_8$ , as obtained from the 2PCF and the 3PCF. We show here the results from the G2 sample only, since they are representative of the generality of the results. In Fig. C1, we show the average and rms scatter over the 153 mocks of the value of  $f\sigma_8$  estimated using the 2PCF and

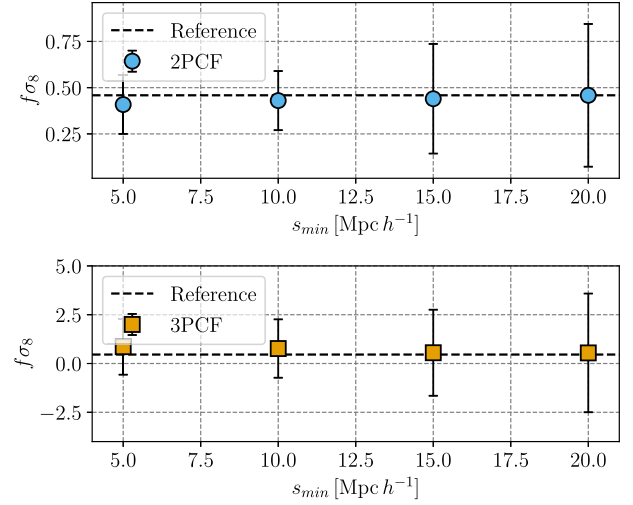


**Figure C1.** Average estimates over the 153 mock samples of  $f\sigma_8$  using the 2PCF (top, filled circles) and the 3PCF (bottom, filled squares), as a function of the minimum scale included in the analysis,  $s_{\text{min}}$ . The black dashed line in both cases gives the reference value, corresponding to the cosmology of the simulated mocks, while error bars are given by the scatter among the mocks. Note how the error bars for the 3PCF estimates are  $\sim 10$  times larger than those from the 2PCF, due to the fact that for the latter only the monopole (i.e. the isotropic information) has been considered.

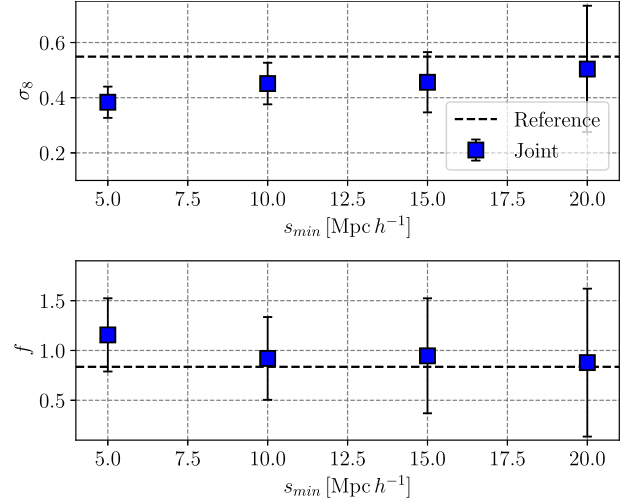


**Figure C2.** Average estimates of  $f(z)$  and  $\sigma_8(z)$  from the joint 2PCF–3PCF analysis of the 153 mocks (filled blue squares), compared to the reference cosmology (black dashed line). As usual, error bars are the standard deviation over the mocks. While the estimates of  $f(z)$  are robust, recovering the input value of the mocks, there is a small bias for  $\sigma_8$  (still within  $1\sigma$  at the reference  $s_{\text{min}} = 15 h^{-1}$  Mpc).

the 3PCF (top and bottom panels, respectively), as a function of  $s_{\text{min}}$ . The results show that including scales as small as  $5 h^{-1}$  Mpc significantly reduces the statistical error without compromising the accuracy. This conclusion is true for both the 2PCF and the 3PCF cases, indicating that the models we have used are adequate for measuring this parameter combination.

Things are different when one tries to break the parameter degeneracy through the joint 2PCF and 3PCF analysis, as shown in Fig. C2. In the two panels, the average estimates of  $\sigma_8$  (top)

and  $f$  (bottom) are plotted as a function of  $s_{\min}$ . Note how the size of the error bars decreases, when smaller scales are progressively included in the analysis. For  $s_{\min} = 5 h^{-1}$  Mpc they are significantly smaller than in our baseline case ( $s_{\min} = 15 h^{-1}$  Mpc). However, while random errors decrease, systematic errors increase: the value of  $\sigma_8$  is systematically underestimated in general (although at the  $1\sigma$

level only) and, to compensate, the measured growth rate is larger than the true one. These results justify our conservative choice to set  $s_{\min} = 15 h^{-1}$  Mpc and indicate that a better modelling is required to push a joint 2PCF and 3PCF analysis to smaller scales.

This paper has been typeset from a  $\text{\TeX}/\text{\LaTeX}$  file prepared by the author.